Valence-Ordered Thin-Film Nickelate with Tricomponent Nickel Coordination Prepared by Topochemical Reduction

Aravind Raji, Zhengang Dong, Victor Porée, Alaska Subedi, Xiaoyan Li, Bernat Mundet, Lucia Varbaro, Claribel Domínguez, Marios Hadjimichael, Bohan Feng, et al.

Valence-Ordered Thin-Film Nickelate with Tri-component Nickel Coordination Prepared by Topochemical Reduction

Aravind Raji[1,2,9], Zhengang Dong[3,4,9], Victor Porée[2], Alaska Subedi[5], Xiaoyan Li[1], Bernat Mundet[6,7], Lucia Varbaro[6], Claribel Domínguez[6], Marios Hadjimichael[6], Bohan Feng[3,4], Alessandro Nicolaou[2], Jean-Pascal Rueff[2], Danfeng Li[3,4,⋆], and Alexandre Gloter[1,⋆]

[1]Laboratoire de Physique des Solides, CNRS, Université Paris-Saclay, Orsay, 91400, France

[2]Synchrotron SOLEIL, L'Orme des Merisiers, BP 48 St Aubin, Gif sur Yvette, 91192, France

[3]Department of Physics, City University of Hong Kong, Kowloon, Hong Kong

[4]City University of Hong Kong Shenzhen Research Institute, Shenzhen, Guangdong, 518057, China

[5]CPHT, Ecole Polytechnique, Palaiseau cedex, 91128, France

[6]Department of Quantum Matter Physics, University of Geneva, Geneva, Switzerland

[7]Electron Spectrometry and Microscopy Laboratory (LSME), Institute of Physics (IPHYS), Ecole Polytechnique Fédérale de Lausanne (EPFL), Lausanne, Switzerland

[8]LCPMR, Sorbonne Université, CNRS, Paris, 75005, France

[9]These authors contributed equally to this work

ABSTRACT: The metal-hydride-based "topochemical reduc-tion" process has produced several thermodynamically unstable phases across various transition metal oxide series with unusual crystal structures and nontrivial ground states. Here, by such an oxygen (de-)intercalation method we synthesis a samarium nickelate with ordered nickel valences associated with tri-component coordination configurations. This structure, with a formula of $Sm_9Ni_9O_{22}$ as revealed by four-dimensional scanning transmission electron microscopy (4D-STEM), emerges from the intricate planes of $\{303\}_{pc}$ ordered apical oxygen vacancies. X-ray spectroscopy measurements and ab initio calculations show the coexistence of square planar, pyramidal, and octahedral Ni sites with mono-, bi-, and tri-valences. It leads to an intense orbital polarization, charge-ordering, and a ground state with a strong electron localization marked by the disappearance of ligand–hole configuration at low temperature. This nickelate compound provides another example of previously inaccessible materials enabled by topotactic transformations and presents an interesting platform where mixed Ni valence can give rise to exotic phenomena.

The on-demand design of transition-metal oxides (TMOs) with emerging properties is imparted by the multivalent nature of the transition-metal ions and the accessible complexity of lattice structures.[1,2] Varying the structure and constituent elements in TMO allows access to a range of competing ground states and exotic electronic landscapes, in which the interplay of the transition-metal orbitals and the connecting oxygen network often plays an essential role.[3] One phenomenal example is the cuprate family, where different coordinational Cu−O frameworks lead to distinctive T_c (T_c, superconducting transition temperature) values.[4] In addition, the fast developments in topotactic soft-chemistry approaches have enabled the synthesis of unconventional TMO with unusual valence states and/or oxygen connectivity.[5−7] One of the recent seminal examples is the synthesis of a family of superconducting low-valence nickelates[8−11] by a topotactic reduction process, which displays intriguing analogies and distinctions to the high-T_c cuprates and is the focus of the current extensive research.

Nickel oxides or nickelates form a large family of structures with diverse crystalline configurations and electronic properties. Perovskite rare-earth nickelates $RNiO_3$ have a rich phase diagram generated by changing the rare-earth cation. They exhibit metal-to-insulator, magnetic, and structural transitions,[12−14] and upon stoichiometry alteration such as oxygen deintercalation or protonization can become reconfigurable neuromorphic devices.[15] Upon a strong topotactic oxygen reduction, $RNiO_2$ infinite-layer nickelates can be obtained, which have recently been discovered as superconducting after hole-doping.[8] While the origin of most of these properties is not yet fully understood, the interplay of spin, charge, and

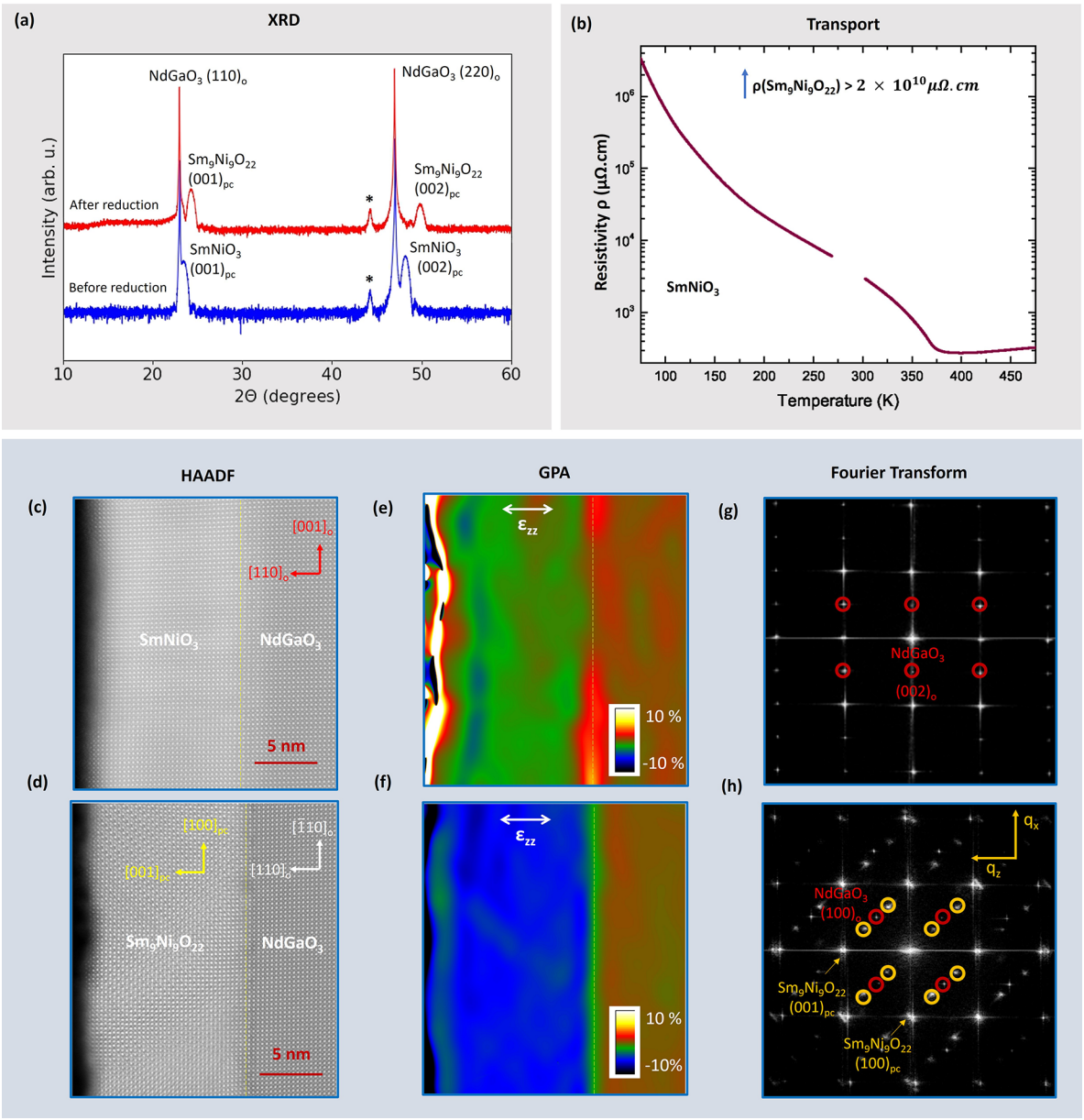

Figure 1. Structural and transport comparison of $SmNiO_3$ with $Sm_9Ni_9O_{22}$ by XRD, HAADF-STEM imaging, GPA, and FT. (a) XRD comparison of both. The 001 and 002 peaks for $SmNiO_3$ occur at lower 2θ values compared to the 001 and 002 peaks of $Sm_9Ni_9O_{22}$, indicating an out-of-plane (o-o-p) compression of the pseudocubic (pc) unit cell upon reduction. Note that the artifact peaks labeled by asterisk are from the diffractometer. (b) Transport measurement of parent $SmNiO_3$ in increasing and decreasing temperatures. The resistivity curve of $Sm_9Ni_9O_{22}$ is not included in the plot since it was significantly higher and is beyond the detection range of the equipment ($>2 \times 10^{10}$ $\mu\Omega$·cm). (c) HAADF-STEM image of $SmNiO_3$ thin film. (d) HAADF-STEM image of $Sm_9Ni_9O_{22}$ thin film, showing in good contrast the stripes coinciding with the $(303)_{pc}$ direction. (e and f) Maps of the o-o-p strain by GPA in (e) $SmNiO_3$ and (f) $Sm_9Ni_9O_{22}$. Both samples show uniform o-o-p compression. $Sm_9Ni_9O_{22}$ exhibits a more negative ϵ_{zz} compared to $SmNiO_3$, corresponding to a lower o-o-p parameter. (g and h) Corresponding FT of the HAADF image of (g) $SmNiO_3$ and (h) $Sm_9Ni_9O_{22}$. The NGO substrate is indexed with an orthorhombic unit cell, and the superstructure spots associated with the tilt pattern of the NGO are encircled in red. The superstructure spots associated with the $(303)_{pc}$ stripes in $Sm_9Ni_9O_{22}$ are encircled in yellow and are indexed within a pseudocubic unit cell.

orbital degrees of freedom is known to drive these exotic properties, along with the associated crystalline configurations.

In the case of infinite-layer nickelate superconductors, a structurally perfect infinite-layer thin film is essential to achieve superconductivity.[16] The topotactic reduction method for infinite-layer nickelate synthesis involves metal hydride, e.g., CaH_2, to remove the apical oxygens from a perovskite nickelate. This often results in a mixture of secondary phases with partial removal of apical oxygen.[17,18] This is due to the partial instability attributed to the infinite-layer structure that does not host Ni^{2+} ($3d^8$) but a Ni^{1+} in a $3d^9$ configuration.[19] Along with superconductivity, the observed charge ordering (CO)[20−23] in these systems now appears to be connected to a structural reordering due to oxygen intercalation in the apical sites.[24,25] Nevertheless, the structure of the charge-ordered systems cannot be directly related to known phases, such as brownmillerite[17] or octahedra and square planar bearing $R_3Ni_3O_7$ phase where Ni^{2+} is absent.[26] The complex transport

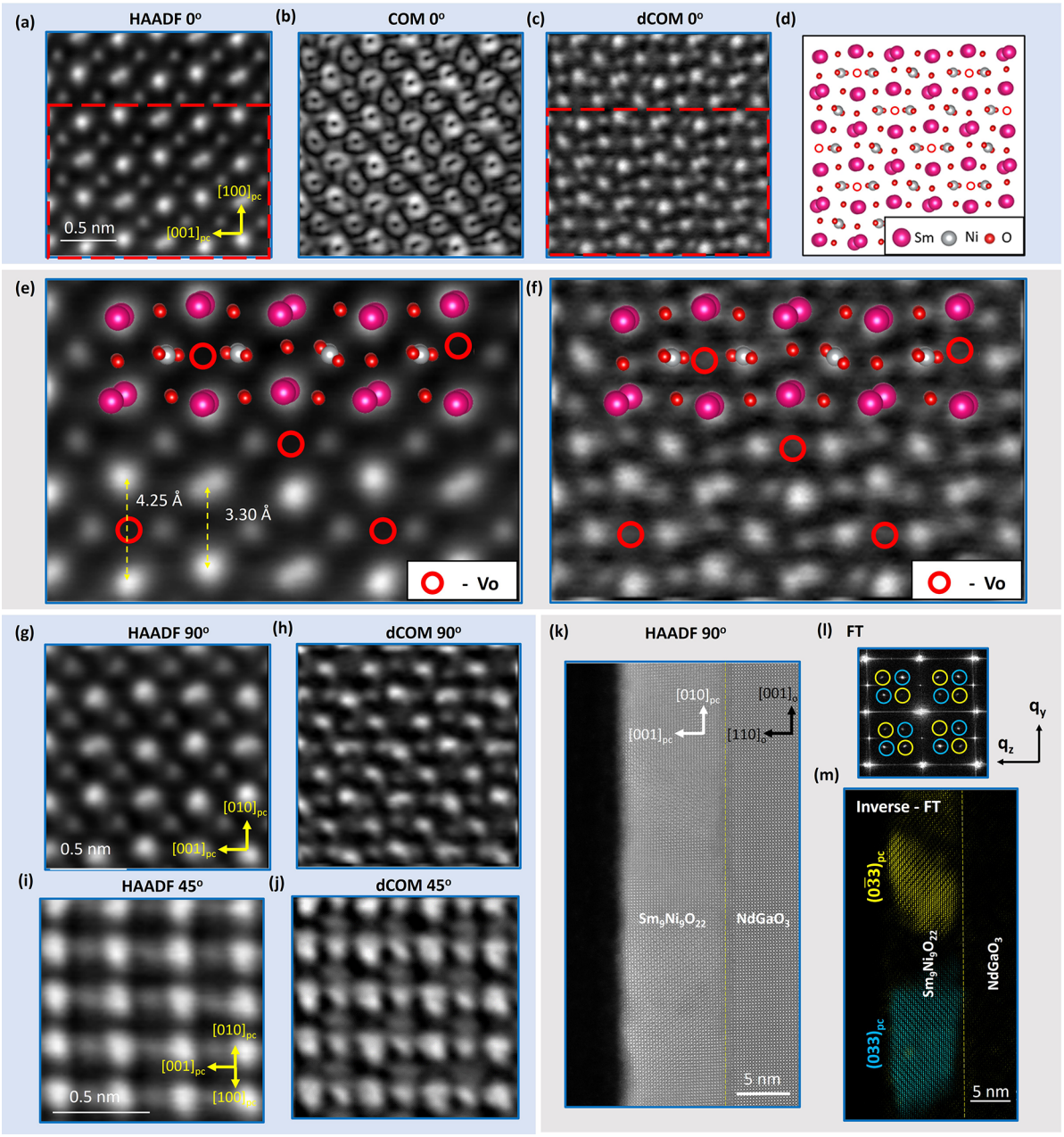

Figure 2. 4D-STEM analysis of $Sm_9Ni_9O_{22}$ in 0, 90, and 45° orientations that correspond to [010], [100], and $[110]_{pc}$ viewing axes. (a) HAADF image of $Sm_9Ni_9O_{22}$ viewed along [010], showing doubled rare-earth sites and elongated−shortened Sm−Sm distances. (b) Absolute intensity COM image of the same region, obtained by 4D-STEM analysis. (c) Corresponding dCOM image, with a very good oxygen phase contrast, that shows the Vo line between the extended Sm−Sm distance, hence along the stripes. (d) Relaxed structural model that is identical to the dCOM image in panel c. (e) Magnified HAADF image of region highlighted in panel a, indicating the location of each atom and showing the extended and reduced regions with and without Vo. (f) Magnified dCOM image of region highlighted in panel c, indicating the location of each atom, and periodic Vo. (g) HAADF image of $Sm_9Ni_9O_{22}$ viewed along [100], showing features similar to those in the view along [010]. (h) Corresponding dCOM image. (i) HAADF image of $Sm_9Ni_9O_{22}$ viewed along [110]. (j) Corresponding dCOM image. (k) Low-magnification HAADF image of $Sm_9Ni_9O_{22}$ viewed along [100], that shows stripes along $(033)_{pc}$ and $(0\bar{3}3)_{pc}$ directions. (l) Corresponding FT showing spots at Q = $(0, \pm\frac{1}{3}, \pm\frac{1}{3})$, $(0, \pm\frac{2}{3}, \pm\frac{2}{3})$, $(0, \pm\frac{1}{3}, \mp\frac{2}{3})$, $(0, \pm\frac{2}{3}, \mp\frac{1}{3})$ reciprocal lattice units (rlu) and Q = $(0, \pm\frac{1}{3}, \pm\frac{2}{3})$, $(0, \pm\frac{2}{3}, \pm\frac{1}{3})$, $(0, \pm\frac{1}{3}, \mp\frac{1}{3})$, $(0, \pm\frac{2}{3}, \mp\frac{2}{3})$ rlu. (m) Inverse-FT image showing the two domains obtained from the highlighted spots in panel l.

properties and notably the unusual dramatic resistivity increase upon oxygen deintercalation of the perovskite nickelates $RNiO_3$ is also intriguing.[27]

This concomitance indicates the possible existence of an unknown stable intermediate phase with multivalent, strong electron localization and charge ordered ground state between the perovskite ABO_3 and the infinite-layer ABO_2.

Here, we demonstrate that the topochemical reduction of a perovskite $SmNiO_3$ thin film grown on an orthorhombic $NdGaO_3$ substrate stabilizes to such an intermediate phase

whose stoichiometry is derived as $Sm_9Ni_9O_{22}$. This ubiquitous phase existing between the much pronounced perovskite ABO_3 and the infinite-layer ABO_2 nickelates hosts intriguing properties associated with multivalent and multicomponent coordinated Ni sites. Intriguing properties of this phase include a strong-orbital polarization, temperature dependent carrier localization, and charge ordering. The observed structural and electronic properties from microscopy and spectroscopy are validated by ab initio simulations, contributing to a coherent analysis and uncovering some regions of its possibly rich phase diagram.

RESULTS AND DISCUSSIONS

Origin of Phases from the $\{303\}_{pc}$ Apical Oxygen Vacancy ordering. We begin with a macroscopic comparison between the parent perovskite $SmNiO_3$ and the reduced $Sm_9Ni_9O_{22}$ thin films, using X-ray diffraction (XRD) and transport measurements. As shown in Figure 1a, we find that the reduction of $SmNiO_3$ results in a scaling down of the pseudocubic (pc) out-of-plane (o-o-p) lattice parameter from 3.78 to 3.63 Å, indicative of a structural transition to the reduced $Sm_9Ni_9O_{22}$ phase. The quality of the thin film is confirmed by the intense Bragg peaks in the XRD scans and the finite-size oscillations in the X-ray reflectivity scans (not shown here). Additionally, in the transport measurements shown in Figure 1b, $SmNiO_3$ evidence a semiconducting behavior with an increase in conductivity of 4 orders of magnitude between 75 K and room-temperature, and a metal-to-insulator transition around 375 K. This is in agreement with previous reports on $SmNiO_3$ thin films.[28] On the other hand, the resistivity of $Sm_9Ni_9O_{22}$ was above the measurement range $> 2 \times 10^{10}$ $\mu\Omega$·cm making it highly insulating with respect to its parent phase.

The microscopic characterization begins with a structural comparison between the parent perovskite $SmNiO_3$ and the reduced $Sm_9Ni_9O_{22}$ thin films, using high-angle annular dark-field (HAADF)-STEM imaging, geometrical phase analysis (GPA),[29] and Fourier transform (FT) analysis. As shown in Figure 1c,d, the HAADF-STEM image shows homogeneous thin films for both $SmNiO_3$ and $Sm_9Ni_9O_{22}$, with a coherent growth obtained on the $(110)_o$ cut $NdGaO_3$ substrate (where subscript "o" stands for the orthorhombic unit cell in the *Pbnm* space group with a = 5.433 Å, b = 5.504 Å, and c = 7.716 Å. In pseudocubic notation, this would be $a_{pc} = b_{pc}$ = 3.86 Å and c_{pc} = 3.858 Å.). Panels e and f of Figure 1 show the maps of o-o-p strain from GPA analysis. The $SmNiO_3$ films have a uniform o-o-p reduction of 3% as compared to the substrate, corresponding to a pseudocubic o-o-p parameter of 3.78 Å (for additional structural details, see Supporting Information, Section 1). On the other hand, the $Sm_9Ni_9O_{22}$ films have a uniform pseudocubic o-o-p parameter of 3.63 Å. Such uniformity indicates a high crystalline quality devoid of any defects, which is also visible at a larger field of view (see Supporting Information, Figure S1). Furthermore, $Sm_9Ni_9O_{22}$ have faint but robust contrasts corresponding to $(303)_{pc}$ oriented stripes which result in superstructure spots in the Fourier transform (FT) shown in Figure 1h at $Q = (\pm\frac{1}{3}, 0, \pm\frac{1}{3})$, $(\pm\frac{2}{3}, 0, \pm\frac{2}{3})$, $(\pm\frac{1}{3}, 0, \mp\frac{2}{3})$, $(\pm\frac{2}{3}, 0, \mp\frac{1}{3})$ rlu. Here we define the reciprocal lattice units (rlu), with in-plane components $a_{pc} = b_{pc}$ = 3.86 Å (constrained by the NGO substrate) and the o-o-p lattice constant c_{pc} = 3.63 Å for the $Sm_9Ni_9O_{22}$.

Complementary 4D-STEM measurements were carried out to further structurally characterize this phase ($Sm_9Ni_9O_{22}$) and determine the local structural modifications at the atomic level. Figure 2 shows the HAADF and 4D-STEM results obtained along different crystallographic orientations of the $Sm_9Ni_9O_{22}$. In Figure 2a,e are the $Sm_9Ni_9O_{22}$ HAADF images at higher magnification, corresponding to a projection of the NGO substrate along the $[001]_o$ zone axis. This is denoted as the 0° projection, or $[010]_{pc}$ zone axis, for the $Sm_9Ni_9O_{22}$ phase. The HAADF image shows the extended and reduced Sm−Sm distances, and one-third of the Sm column exhibits a doubling, with all of these reconstructions running periodically along the $\{303\}_{pc}$ stripes. 4D-STEM data collected simultaneously with the HAADF images are shown in Figure 2c,f. Figure 2b corresponds to the displacement intensity of the center-of-mass (COM) of the diffraction plane collected at every probe position, and donut shapes reveal the presence of atomic columns at their centers, even for oxygen atoms.[30,31] Indeed, the lateral momentum transfer to the electron beam (Δp) is determined from these center-of-mass measurements. This Δp is negatively proportional to the in-plane electric field E, thereby making Figure 2b a rough representation of in-plane electric field absolute intensity as well. The centers of the donut indicate then the presence of an atomic columns. Furthermore, the Figures 2c,f, can be considered as the divergence of in-plane electric field, thus approximating the projected charge-density image, with extrema located at the atomic positions. These images reveal unambiguously that columns of apical oxygen vacancies (Vo) are ordered along the stripes. This is causing the rare-earth superstructure, since the Sm atoms are moving away from the Vo sites giving separations between the Sm atoms of ≈4.25 Å as shown in Figure 2e, while a reduced separation of ≈3.30 Å is measured when columns of apical oxygen are preserved. See Supporting Information, section 2 for these parameters in the structural models. Such local variations in the A-cation distances, arising due to the coexistence of different coordinations of B sites have been observed in studies of cobaltite,[32] ferrite,[33] and manganite[34] systems.

A structural model showing a similar atomic reconstruction is shown in Figure 2d. This was obtained by an ab initio crystal relaxation of a cubic $SmNiO_3$, after introducing a single family of $(303)_{pc}$ planes of apical Vo. The presence of such planes of Vo leads to a mixture of octahedral and pyramidal Ni sites, and it forms the n = 3 member of a family made of $(n0n)_{pc}$ planes of Vo, with a formula $A_nB_nO_{3n-1}$. Interestingly, infinite-layer nickelates, with the formula $RNiO_2$ form the n = 1 member. The structural details of such $A_nB_nO_{3n-1}$ series as predicted by ab initio calculations are in Supporting Information, section 2.1.

The STEM images measured along a projection rotated by 90° compared to Figure 2a (corresponding to a substrate $[\bar{1}10]_o$ zone axis and a $[100]_{pc}$ $Sm_9Ni_9O_{22}$ zone axis) as shown in Figure 2g,h indicate that the vacancy ordering is taking place along two perpendicular projections. While the observation along the 0° projection of the $Sm_9Ni_9O_{22}$ was only showing $(303)_{pc}$ planes (e.g., and not a $(\bar{3}03)_{pc}$), panels k−m of Figure 2 show different domains in 90° projections, where the stripes coincide with the $(033)_{pc}$ or the $(0\bar{3}3)_{pc}$ planes. This indicates that 0 and 90° projections are not exactly symmetrical, which is most likely due to the orthorhombicity of the substrate, that causes an asymmetry between the two in-plane directions.

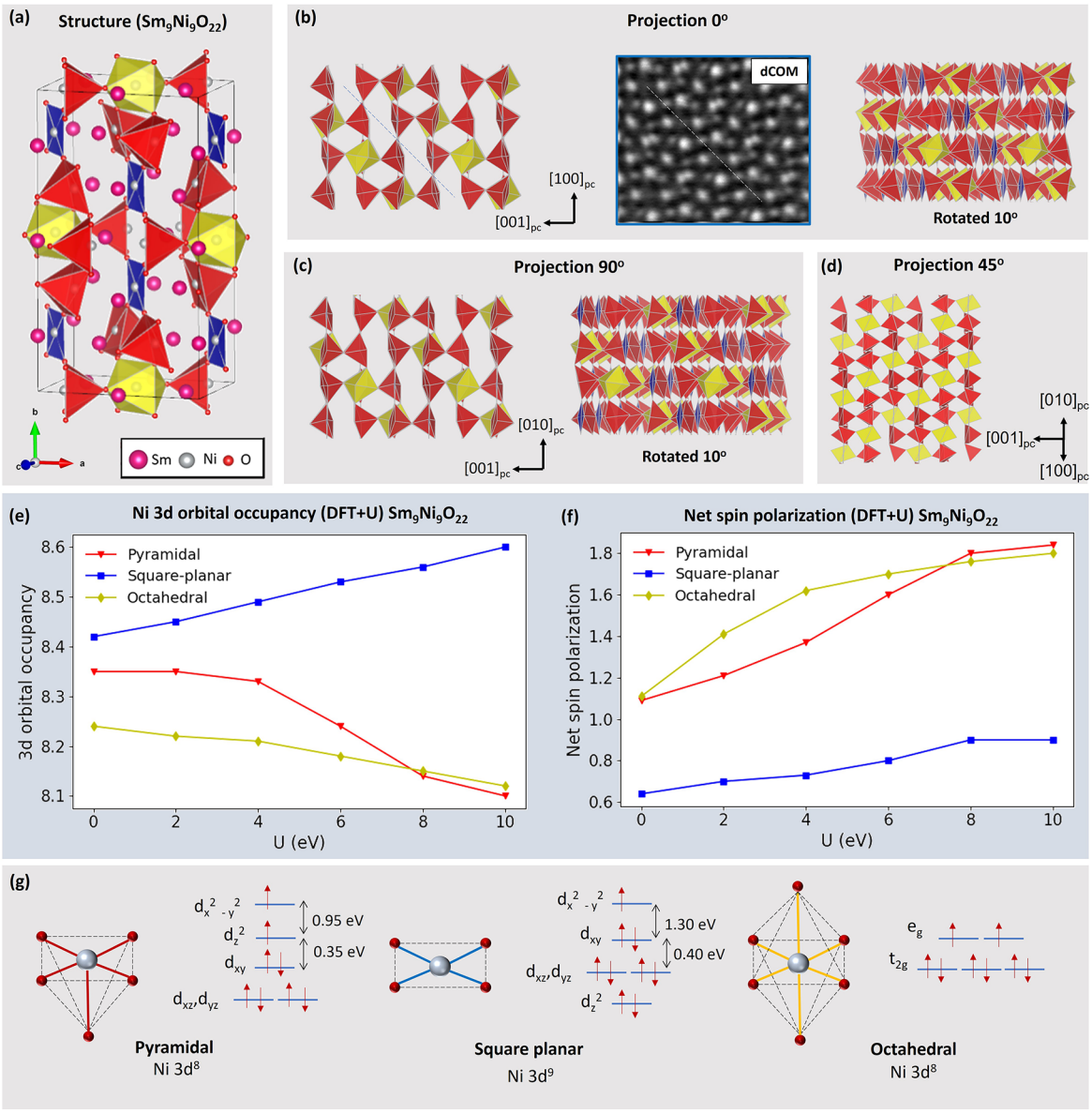

Figure 3. Structural and electronic refinements by DFT. (a) Relaxed structural model of $Sm_9Ni_9O_{22}$, with Ni sites in a mixed coordination of pyramidal, square planar, and octahedral. The axis indicated in this figure is the local axis with respect to the structure symmetry. (b) Polyhedral distribution viewed along $[010]_{pc}$ and a 10° rotation along [100], with the area matching with that of the dCOM image. (c) Polyhedral distribution viewed along $[100]_{pc}$ and a 10° rotation along [010]. (d) Polyhedral distribution viewed along [110]. From viewing along the three projections, the different polyhedra appear to have a periodic distribution. (e) Calculated 3d orbital occupancy of different Ni sites for U = 0−10 eV by DFT+U. (f) Calculated net spin polarization of different Ni sites for U = 0−10 eV by DFT+U. (g) Demonstration of the d-orbital occupancy of different Ni sites. Ni in the pyramidal and octahedral sites are in a $3d^8$ configuration, while Ni in the square planar sites are in a $3d^9$ configuration.The indicated orbital energy differences are obtained from the calculated values from the RIXS fit, as indicated in Supporting Information, Table S3.

Nevertheless, locally both orientations reveal very similar cation and oxygen atomic reconstruction of the $Sm_9Ni_9O_{22}$. This essentially identifies that this phase is obtained by intersecting apical Vo planes of $(303)_{pc}$ and $(033)_{pc}$ orientations. Such a possible tetragonal symmetry is also confirmed by the observation along 45° projection as shown in Figure 2i,j. The apical oxygen removal indicatively reduces the o-o-p parameter, as is the case for infinite-layer nickelates, where the complete removal of apical oxygen results in an o-o-p parameter of ≈3.30 Å.[8,35−37] The observed o-o-p parameter of 3.63 Å in $Sm_9Ni_9O_{22}$ is thus associated with these oxygen deficiencies.

Structural and Charge Ordering from Ab Initio Calculations. From these microscopic results, it is evident that this phase cannot be simply explained by one family of Vo planes, and intersecting $(303)_{pc}$ and $(033)_{pc}$ planes of apical vacancies are needed. Corresponding simulations involved the structural relaxations of a 6 × 6 × 6 cubic $SmNiO_3$ supercell with $(303)_{pc}$ and $(033)_{pc}$ ordered apical Vo. The substrate constrained calculations resulted in a tetragonal structure with an o-o-p parameter of c_{pc} = 3.63 Å. This 6 × 6 × 6 tetragonal supercell was then symmetrized, giving an 80-atom structure with the formula $Sm_{18}Ni_{18}O_{44}$, as shown in Figure 3a, which can be further shortened as $Sm_9Ni_9O_{22}$. More details are given

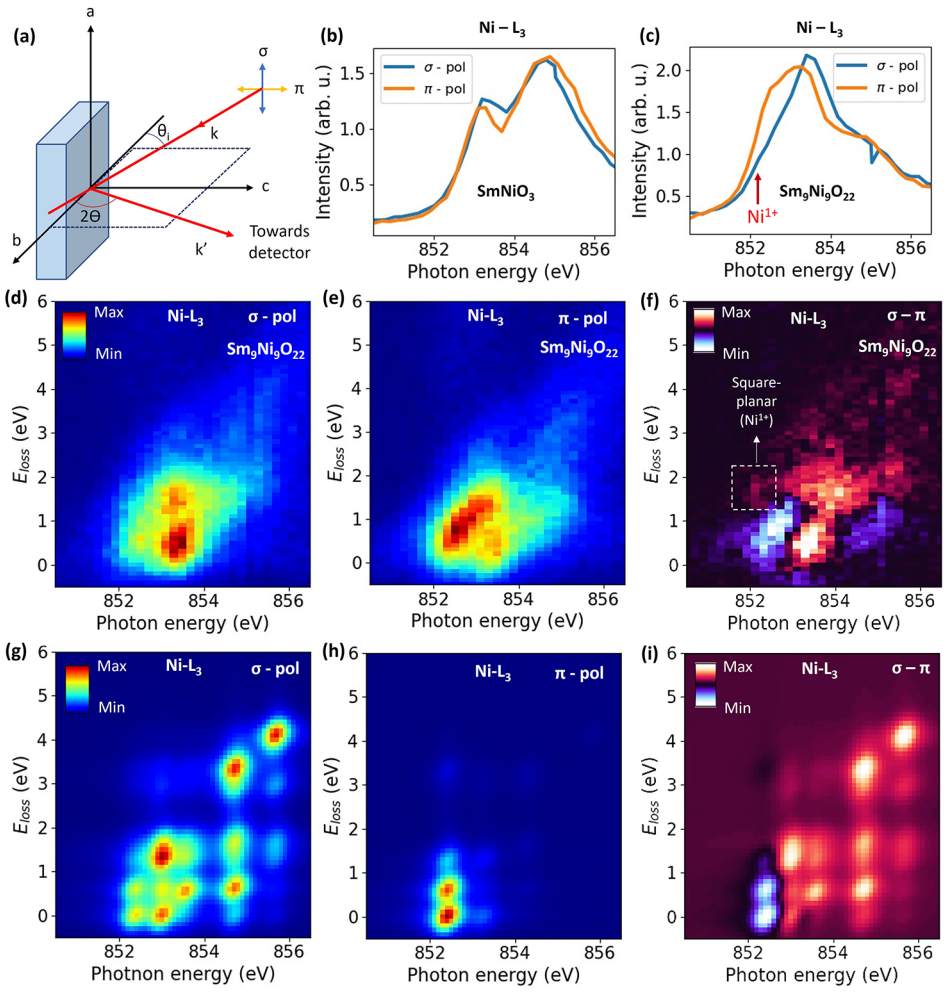

Figure 4. Electronic structure analysis by XAS and RIXS. (a) Experimental geometry showing the incident X-ray polarizations σ and π, incident X-ray angle θ_i, and the scattering angle 2Θ. (b and c) XAS partial fluorescence yield (PFY) spectra at 25 K at Ni-L_3 edge of (b) $SmNiO_3$ and (c) $Sm_9Ni_9O_{22}$. (d and e) Ni-L_3 edge RIXS map at 25 K of $Sm_9Ni_9O_{22}$ in (d) σ—incident polarization—and (e) π—incident polarization of the photons. (f) Difference of RIXS map between the two polarizations. (g and h) Calculated Ni-L_3 edge RIXS map of Ni^{2+} pyramidal sites, in (g) σ-polarization and (h) π-polarization.(i) Difference of calculated RIXS map between the two polarizations.

in Experimental Section and Supporting Information, section 2. This structure essentially identifies three types of Ni sites: NiO_6 octahedral (Oh), NiO_4 square-planar (Sq), and NiO_5 pyramidal (Py) in the ratio 1:2:6 in the lattice. In this regard, it is very different from the $A_3B_3O_7$,[26] which have the Vo in the periodicity $\frac{1}{3}$ from the parent ABO_3 structure and is built with apical Vo lines running only along one projection. It is here also noted that an alternative $A_3B_3O_7$ structure can also been obtained by mixing apical Vo $(303)_{pc}$ planes and equatorial Vo $(033)_{pc}$ planes, but the resulting structure would not match our observation (see Supporting Information, Figure S5).On the grounds of differently coordinated Ni sites in the lattice, a mixed valence is expected for the $Sm_9Ni_9O_{22}$ composition. Ab initio calculations give evidence of different Ni electronic configurations for the different site coordination as indicated by Figure 3e–g. Calculations have been done including a Hubbard U parameter ranging from 0 to 10 eV, as shown in Figure 3e,f. At U = 0 eV, differences of total charges on the Ni sites are already present but become more segregated between the square and the octahedra or the pyramid when U increases. The Ni in square planar sites are in a $3d^9$ configuration, indicating Ni^{1+} and a spin = 1/2 (typical occupation matrix is given in Supporting Information, Table S2). The Ni in the pyramidal and octahedral sites are closer to a $3d^8$ configuration and a spin = 1. A $Sm_9Ni_9O_{22}$ composition would imply 17 charges to be distributed over the nickel sites and a possible distribution would then be 2 sq(Ni^+, d^9), 6 Py(Ni^{2+}, d^8) and a single Oh (Ni^{3+}, $3d^8\underline{L}$ with $\underline{L}$ referring to a hole in the ligand). The exact nature of the Ni^{3+} ground state (i.e., the respective weight of $3d^7$ and $3d^8\underline{L}$ in the ground state) is difficult to address solely based from the DFT+U level where, in brief, electron localization and correlation are brutally parametrized. We also assume that a ligand hole will reside on the octahedral sites by analogy from the electronic structure of the parent $SmNiO_3$ phase. In the metallic state, it is known to host octahedral Ni^{3+} with primary covalent ground state (a.k.a, as negative charge transfer), id est, primarily composed by a $3d^8\underline{L}$. In the insulating state, the bond disproportionates with the presence of collapsed $d^8\underline{L}^2$ and expanded d^8 octahedral sites.[38] These charge distribution and orbital physics are summarized in Figure 3g, and they are further probed by spectroscopic techniques involving X-ray absorption spectroscopy (XAS), resonant inelastic X-ray scattering (RIXS) and hard X-ray photoemission spectroscopy (HAXPES).

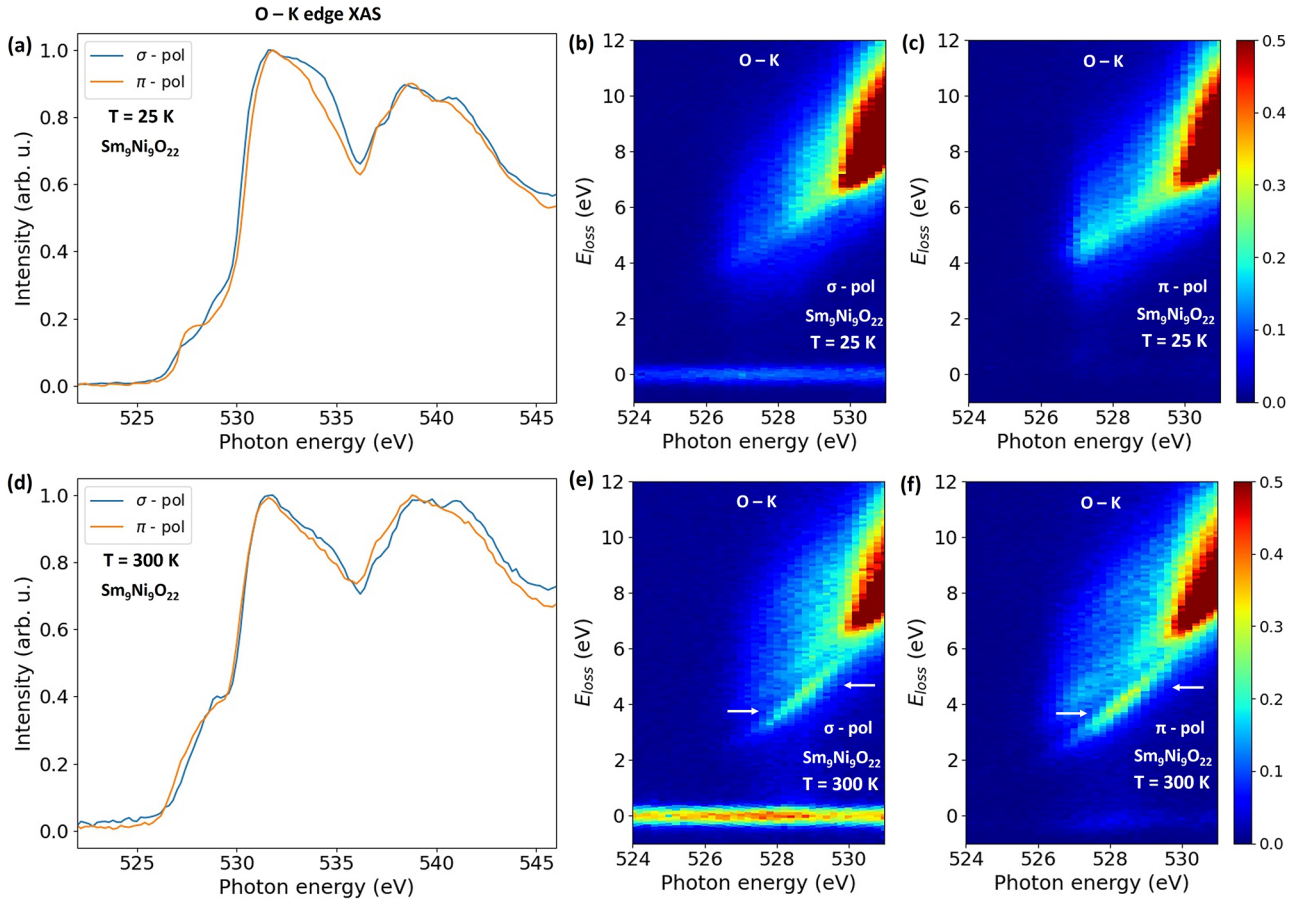

Figure 5. Temperature dependent spectroscopic studies at the O-K edge by XAS and RIXS maps (in energy loss) of $Sm_9Ni_9O_{22}$. (a–c) Measurements at T = 25 K, (a) O-K edge PFY XAS spectra in σ and π incident polarizations. (b and c) RIXS map at O-K edge for (b) σ incident photon polarization and (c) π incident photon polarization. (d–f) Measurements at T = 300 K, (d) O-K edge PFY XAS spectra in σ and π incident polarizations, (e and f) RIXS map at O-K edge for (e) σ incident photon polarization and (f) π incident photon polarization. A low energy fluorescence line emerges at 300 K, as indicated by white arrows in the RIXS spectra.

Orbital Polarization and Charge Localization by Spectroscopic Measurements. The schematic of the XAS and RIXS measurements using a linearly polarized beam is briefly indicated in Figure 4a. The XAS Ni-L_3 edge of the parent perovskite $SmNiO_3$ thin film measured at 25K is given in Figure 4b which shows a typical splitting associated with bond disproportionation and the presence of collapsed $d^8\underline{L}^2$ and expanded d^8 octahedra for the insulating state.[38] A more complete set of the XAS and RIXS data at the Ni-L edges measured for the parent $SmNiO_3$ thin film at RT (300 K) and 25 K can be seen in Supporting Information, Figure S7. They are in agreement with previously reported spectroscopic work on perovskite nickelate thin films,[39] and they show a fully developed insulating behavior at 25 K, and a partial metal-to-insulator transition occurring at RT (300 K) as revealed by a blurring of the XAS Ni-L_3 edges together with a blue shift of the localized dd-orbital excitations in the RIXS.[39] More discussion on this aspect is given in Supporting Information, Section 3. The Ni-L_3 edge XAS for the $Sm_9Ni_9O_{22}$ sample (Figure 4c) occurs at a lower excitation energy than that of $SmNiO_3$ indicating a reduced valence toward Ni^{2+} and Ni^{1+} as it was inferred from the structural investigation. In complement, a Ni $2p_{3/2}$ and Ni $2p_{1/2}$ core level bulk sensitive HAXPES measurements between $Sm_9Ni_9O_{22}$ and $SmNiO_3$ are given in Supporting Information, Figure S13 that shows a similar valence trend. Here, in Figure 4c, a strong dichroism is observed at the Ni-L edges of the $Sm_9Ni_9O_{22}$ with a noticeable o-o-p higher intensity (corresponding to π-polarization) at the low-energy side of the Ni-L_3 main edge (at 852.5 eV). From atomic multiplet calculations (shown in Supporting Information, Section 4),[40] this strong dichroism is considered to be stemming from the Ni^{2+} in the pyramidal sites, which are the most populated in the lattice. By projecting the XAS final-state $2p^53d^9$ in terms of crystal field configuration, the features at 852.5 and 853.3 eV are identified respectively with $3d_{z^2-r^2}$ and $3d_{x^2-y^2}$ symmetry of the pyramidal sites explaining the sign and the hierarchy of the X-ray linear dichroism (XLD) signal.[40,41] An in-plane contribution is also expected from the XAS spectra of the square planar $3d_{x^2-y^2}$ state of the Ni^{1+}, and it is at the origin of the shoulder observed at 852.3 eV for the σ-polarization. Nevertheless, the overall shape of the XAS-XLD is dominated by the Ni^{2+} in the pyramidal site with only a smaller contribution of the Ni^{1+} site in the square plane. These multivalent features of the $Sm_9Ni_9O_{22}$ structure are made clearer in the RIXS maps. The data for the σ- and π-polarizations, along with their linear dichroisms, are displayed in Figure 4d–f. The RIXS data show dichroism similar to that observed in XAS, e.g., with a larger contribution in the π-polarization at ≈852.5 eV. The calculated RIXS maps obtained for a Ni^{2+} within a pyramid are in fair agreement with the experimental maps (Figure 4g–i). A noticeable difference on comparing Figure 4f,I is the experimental intensity at an energy

loss of 1.7 eV obtained for an excitation energy of ≈852.3 eV, which is not present in the calculation done for Ni^{2+}. This excitation energy corresponds to Ni^{1+}, and its higher intensity for a σ-polarization is consistent with a square planar symmetry (see calculation in Figure S15), in accordance with $3d_{x^2-y^2} \rightarrow 3d_{xy}$, $3d_{xz}/3d_{yz}$ d−d transitions as also discussed by Rossi et al.[42] in the case of an IL-nickelate. The RIXS signatures have also been investigated at RT for some excitation energies. The dichroic nature of $Sm_9Ni_9O_{22}$ is rather similar at room temperature, as shown in (Supporting Information, Figures S7 and S8), but some d−d transitions experience blue shift of ≈0.2 eV indicating electronic modification between low and room temperature.

In complement, similar spectroscopic studies have been carried out at the O-K edge for the parent and reduced phase, both at low and room temperature. O-K edge XAS has been previously used to investigate the electronic transition in a perovskite nickelate.[43] Here in the parent phase, along with the XAS, the electronic transition is further characterized by the RIXS maps that also indicates a band gap opening at low temperature (Supporting Information, Figures S9 and S10).

The O-K edge XAS and RIXS maps of $Sm_9Ni_9O_{22}$ shown in Figure 5a−f and in Supporting Information, Figures S11 and S12 are very different from the parent $SmNiO_3$. The prepeak of the O-K is very weak, which also confirms a reduced valency and covalency as compared to the Ni^{3+} of $SmNiO_3$. The position of the prepeak also confirms a band gap opening of ≈3 eV for the reduced $Sm_9Ni_9O_{22}$. While being of small intensity, the prepeak shows a strong incident photon polarization dependence. At low temperature, this prepeak has stronger components at energies 527.2 eV for a σ-polarization, then at 527.6 eV for a π-polarization and at 528.9 eV for a σ-polarization that could be interpreted by a combination of hybridization of the O-2p orbital with the unoccupied $3d_{x^2-y^2}$ of the Ni^{1+} and then with the $3d_{z^2}$ and $3d_{x^2-y^2}$ of the Ni^{2+}. This goes hand in hand with the respective energy positions of the calculated unoccupied density of states of these orbitals as shown in (Supporting Information, Figure S16).

The XAS O-K pre-edge at room temperature seems smeared out and exhibits a weaker dichroism. While observing the RIXS maps, a strong fluorescence line appears at room temperature causing the blurring of the O-K XAS pre-edge feature. This fluorescence line occurs for an incident photon energy corresponding to Ni−O hybridization and with the smallest energy loss, involving energy bands at the upper part of the valence band. A disappearance with temperature of this fluorescence line reveals an electronic phase transition and somehow a charge localization at low temperature for the $Sm_9Ni_9O_{22}$. Due to the weak dichroic character of this band, the localization might concern the Ni^{3+} in the octahedra whose electron configuration in the parent phase is also prone to charge localization.[44] Futhermore, additional electrons associated with oxygen deficient perovskite nickelates have also been predicted to strongly localize on octahedral sites, explaining the dramatic decrease in the electrical conductivity by several orders of magnitude in them.[27]

CONCLUSIONS

Here, the topotactic reduction of a parent perovskite $SmNiO_3$ thin film grown on $NdGaO_3$ results in a homogeneous thin film of the $Sm_9Ni_9O_{22}$ phase, with in-plane parameters constrained on the substrate and a reduced pseudocubic o-o-p parameter of 3.63 Å. This structure emerges from families of $\{303\}_{pc}$ apical oxygen vacancy (Vo) ordering giving a formula $A_9B_9O_{22}$ as revealed by 4D-STEM. A single family plane will give the $A_3B_3O_8$ phase with only octahedral and pyramidal Ni sites. Here we show that the $A_9B_9O_{22}$ phase emerges from Vo families along two orientations, giving rise to square planar, pyramidal, and octahedral Ni sites. The square planar environment occurs at the intersection of orthogonal families and harbors a Ni^{1+} indicating a possible route to IL-structure. It should be noted that such $(303)_{pc}$ phases have also been reported as structural defects, constrained in a quasi-2D nanosheet on the top of IL-NNO2.[24] In fact, such a $(303)_{pc}$ defect might be present as nanodomains, presumably along a single orientation, or overlap along different orientations and order at longer range as we showed here, enabling phase engineering in the ABO_2−ABO_3 system. In such case, this $A_9B_9O_{22}$ phase could be a member of the family of nickel oxides that forms by $\{n0n\}_{pc}$ ordered Vo. Overlapping $(n0n)_{pc}$ and $(0nn)_{pc}$ apical oxygen vacancy planes result in a general formula $A_{n^2}B_{n^2}O_{3n^2-2n+1}$ that is indeed spanning from the IL-ABO2 with only square planar to the perovskite ABO_3 with only octahedral Ni sites. In-between, octahedral, square planar and pyramidal sites are in the ratio $(n-2)^2$:2:$(4n-6)$. Such $\{n0n\}_{pc}$ planes could be seen as an analogous case of the Ruddlesden−Popper (RP) faults that is also present from the individual 2D defects and scale to a fully developed RP phase.

The stability of this family is still to be understood, and being an intermediate phase, it will depend on epitaxial strain and redox condition. This is in line with our observations indicating that the orthorhombic substrate plays a role, as strain in thin films is generally known to control the creation of Vo, even for the stabilization of superconducting IL-nickelate films.[45] Additionally, the choice of the reducing agent such as CaH_2,[8] alumina[11] and atomic hydrogen[25] can influence the selective stabilization of each phase. The $A_9B_9O_{22}$ phase is also a neighbor of other members of the oxygen deficient nickelate series, such as the brownmillerite $ABO_{2.5}$[17] and the $A_3B_3O_7$.[26] The chemical dynamics behind the selective stabilization of these phases is still not understood. Possibly, this $A_9B_9O_{22}$ phase, that we report here, might have been present along the samples that reported the $A_3B_3O_7$,[35,36] or it might have been misinterpreted as that.

Interestingly, ab initio calculations and spectroscopic studies coherently indicate that the $Sm_9Ni_9O_{22}$ phase consists of tricomponent Ni sites, with a varying valence from Ni^{1+} to Ni^{3+}. Each component is associated with a unique symmetry, charge, orbital, and spin distribution, that collectively express a multivalent character with different degrees of orbital polarization at each site, as evidenced by our spectroscopic studies. The tricomponents are distributed in the lattice with a periodicity determined by the Vo ordering, contributing to a commensurate charge order for this system with a periodicity ($\frac{1}{3}$, 0, $\frac{1}{3}$) rlu. This periodicity is strikingly similar to that of the CO reported in IL-nickelate thin films.[20−23] This possibly indicates the existence of this phase in IL-nickelate thin films as a defect, and this is further strengthened from recent studies reporting apical oxygen ordering in IL-nickelate thin films that exhibited similar CO.[24,25] It questions how intrinsic is the ($\frac{1}{3}$, 0) rlu CO in IL-$NdNiO_2$.

The parent perovskite $SmNiO_3$ exhibits a metal-to-insulator (MIT) around 375 K as evidenced by our transport measurements, and this is similar to what was previously

reported[28] in these. However, the $Sm_9Ni_9O_{22}$ system has a complex multivalent electronic landscape, with an intriguing carrier localization contributing to an enhanced resistivity. This is in contrast with the case of oxide semiconductors, where Vo cause an enhanced conductivity. However, this is in line with previous reports on perovskite nickelates, where the Vo cause localization of electrons at the octahedral Ni sites,[27] with the subsequent filling of the ligand hole resulting in a $3d^8$ configuration. The oxygen deficient nickelate discussed in that report might correspond to this phase. Furthermore, RIXS evidence an additional charge localization at low temperature, presumably associated with the charge configuration at octahedral Ni site. It is worth noting that the Ni sites at the parent phase octahedra have known charge fluctuation $3d^8\underline{L} \leftrightarrow 3d^8 + 3d^8\underline{L}^2$ playing a role in the temperature driven MIT. This might be hindered for an isolated octahedron, giving rise to different charge fluctuation (e.g., $3d^8\underline{L} \leftrightarrow 3d^7$), making the phase diagram of this system more complex.

On a broader perspective, this is another example of the idea of selective oxygen incorporation driving stabilization of phases/interfaces that have metallic, semiconducting, insulating, and even superconducting (with doping) properties.[8,46−48] The carrier distribution in the lattice, which is associated with the distribution of oxygen atoms, has an identical effect as that of hydrogenated perovskite nickelate devices proposed for neuromorphic computing applications.[15] This was demonstrated for an oxygen deficient $NdNiO_{3-\delta}$ nickelate device, that could potentially have this $A_9B_9O_{22}$ phase, where multiple resistance states were achieved by adjusting the electronic bias.[27] Such findings uncover the possible multitude of applications of this phase on par with other strongly correlated electron systems.

EXPERIMENTAL SECTION

Samples. Before growth, the $(110)_o$-oriented $NdGaO_3$ single-crystalline substrates were annealed at 1150 °C for 10 h in flowing oxygen to obtain sharp step-and-terrace surface morphology. Then the pristine 14 nm thick $SmNiO_3$ epitaxial thin films were grown by off-axis radio frequency magnetron sputtering, at a substrate temperature of 460 °C and a total pressure of 0.18 mbar with an oxygen/argon mixture of 1:3.[49] After growth, the samples were cut into pieces with the size of 5 × 2.5 mm^2 and loosely wrapped in the aluminum foil. The wrapped samples were then sealed under vacuum in Pyrex glass tubes, embedded with CaH_2 powder of ≈0.1 g. The sealed glass tubes were heated in a tube furnace to 230−240 °C for 1 h and cooled to room temperature at a rate of 10 °C/min.

High-Resolution HAADF-STEM Imaging and 4D-STEM. Cross-sectional transition electron microscopy (TEM) lamellae were prepared using a focused ion beam (FIB) technique (at C2N, University of Paris-Saclay, France). Before FIB lamellae preparation, around 20 nm of amorphous carbon was deposited on top for protection. The HAADF imaging and 4D-STEM were carried out in a NION UltraSTEM 200 C3/C5-corrected scanning transmission electron microscope (STEM). The experiments were done at 200 keV with a probe current of approximately 10 pA and convergence semiangles of 30 mrad. A MerlinEM instrument (Quantum Detectors Ltd.) in a 4 × 1 configuration (1024 × 256) has been installed on a Gatan ENFINA spectrometer mounted on the microscope.[50] The EELS spectra are obtained using the full 4 × 1 configuration and the 4D-STEM by selecting only one of the chips (256 × 256 pixels). For 4D-STEM, the EELS spectrometer is set into non-energy dispersive trajectories and we have used 6-bit detector mode that gives a diffraction pattern with a good signal-to-noise ratio without compromising much on the scanning speed.

Ab Initio Calculations. The first-principles calculations were performed using the density functional theory[51] as implemented in the Quantum ESPRESSO package.[52,53] The exchange−correlation functional was approximated by the generalized gradient approach.[54] Planewave cutoffs of 40 and 400 Ry were used for basis-set and charge density expansions, respectively. Structural relaxations were done without considering a Hubbard U parameter, while the electronic structure were calculated with it. All DFT+U calculations were performed with a J = 1.2 eV, making $U_{\text{effective}} = U - J$. All structural relaxations begin with creating a supercell from a cubic $SmNiO_3$, with a = 3.80 Å. Then, the oxygen atoms along the corresponding family of Vo planes were removed. For the $Sm_9Ni_9O_{22}$ phase, after removing the two orthogonal families of apical Vo, it results in a 960-atom 6 × 6 × 6 supercell. The resulting pseudotetragonal o-o-p parameter of c = 3.63 Å was obtained by minimizing the total force in a 6 × 6 × 6 supercells (the in-plane pseudotetragonal parameter $a = b$ = 3.90 Å, was frozen). This tetragonal supercell was then reduced using symmetry to an monoclinic 80-atom cell. Thus, the obtained structure has the space group $C2/m$ and lattice parameters of a = 9.02, b = 16.09, c = 6.47 Å, and β = 87.57°. The structural parameters with atomic positions are given in Table S1. The lattice vectors of the tetragonal 960-atom phase ($\vec{a_T}$, $\vec{b_T}$, $\vec{c_T}$) expressed in the symmetrized monoclinic parameters ($\vec{a_m}$, $\vec{b_m}$, $\vec{c_m}$) are $\vec{a_T} = \vec{a_m} + \vec{b_m} + 2\vec{c_m}$, $\vec{b_T} = \vec{a_m} - \vec{b_m} + 2\vec{c_m}$, and $\vec{c_T} = 2\vec{a_m} - 2\vec{c_m}$.

XAS and RIXS Measurements. The X-ray absorption spectroscopy (XAS) and resonant inelastic X-ray scattering (RIXS) measurements of the Ni-L edges and the O-K edge were performed at the AERHA instrument of the SEXTANTS beamline at the SOLEIL synchrotron. A detailed optical scheme of the spectrometer that involves dispersing the X-ray photons as a function of their energy onto a two-dimensional detector is given in ref 55 and the experimental geometry in Figure 4a. The measurements were performed with the a and c sample axes in the horizontal scattering plane. Measurements at the Ni-L and O-K edges were taken with θ_i = 20° (where θ_i is the angle between the incoming X-ray and the sample surface), and linear dichroism was obtained by switching the incident X-ray polarization between σ and π. RIXS was measured at 2Θ = 85°, with an overall full width at half-maximum (fwhm) energy resolution of 170 ± 10 meV for the O-K edge and 300 ± 10 meV for the Ni-L edge. The measurements were done at T = 25 K and T = 300 K. The two-dimensional RIXS data are binned in the isoenergetic direction to form spectra, and the pixel to energy conversion is performed by measuring the position of the elastic line of the spectrometer while changing the beamline energy.

HAXPES Measurements. The measurements were carried out at the GALAXIES beamline at the SOLEIL synchrotron[56] on the HAXPES endstation[57] using a photon energy of 3000 eV, with an incidence angle of 10°. The bulk sensitivity is defined from the SESSA simulations,[58] which give a probing depth of around 10 nm for 10° incidence. About 95% of the detected signal will be from the elements within these estimated probing depths. The synchrotron operated with a ring current of 450 mA, giving an intensity of 3.4 × 10^{13} photons/s at 3000 eV, which was then reduced using a built-in filter to 5% of the original intensity. The photoelectrons were detected using a SCIENTA Omicron EW4000 HAXPES hemispherical analyzer, and a Shirley background[59] was removed prior to fitting the core levels spectra.

AUTHOR INFORMATION

Corresponding Authors

Danfeng Li − *Department of Physics, City University of Hong Kong, Kowloon, Hong Kong; City University of Hong Kong Shenzhen Research Institute, Shenzhen, Guangdong 518057, China;* orcid.org/0000-0001-6894-6765; Email: danfeng.li@cityu.edu.hk

Alexandre Gloter − *Laboratoire de Physique des Solides, CNRS, Université Paris-Saclay, Orsay 91400, France;* orcid.org/0000-0002-4813-3799; Email: alexandre.gloter@universite-paris-saclay.fr

Authors

Aravind Raji − *Laboratoire de Physique des Solides, CNRS, Université Paris-Saclay, Orsay 91400, France; Synchrotron SOLEIL, Gif sur Yvette 91192, France*

Zhengang Dong − *Department of Physics, City University of Hong Kong, Kowloon, Hong Kong; City University of Hong Kong Shenzhen Research Institute, Shenzhen, Guangdong 518057, China*

Victor Porée − *Synchrotron SOLEIL, Gif sur Yvette 91192, France*

Alaska Subedi − *CPHT, Ecole Polytechnique, Palaiseau Cedex 91128, France*

Xiaoyan Li − *Laboratoire de Physique des Solides, CNRS, Université Paris-Saclay, Orsay 91400, France;* orcid.org/0000-0003-2332-2523

Bernat Mundet − *Department of Quantum Matter Physics, University of Geneva, Geneva 1211, Switzerland; Electron Spectrometry and Microscopy Laboratory (LSME), Institute of Physics (IPHYS), Ecole Polytechnique Fédérale de Lausanne (EPFL), Lausanne 1015, Switzerland*

Lucia Varbaro − *Department of Quantum Matter Physics, University of Geneva, Geneva 1211, Switzerland*

Claribel Domínguez − *Department of Quantum Matter Physics, University of Geneva, Geneva 1211, Switzerland*

Marios Hadjimichael − *Department of Quantum Matter Physics, University of Geneva, Geneva 1211, Switzerland*

Bohan Feng − *Department of Physics, City University of Hong Kong, Kowloon, Hong Kong; City University of Hong Kong Shenzhen Research Institute, Shenzhen, Guangdong 518057, China*

Alessandro Nicolaou − *Synchrotron SOLEIL, Gif sur Yvette 91192, France*

Jean-Pascal Rueff − *Synchrotron SOLEIL, Gif sur Yvette 91192, France; LCPMR, Sorbonne Université, CNRS, Paris 75005, France;* orcid.org/0000-0003-3594-918X

ACKNOWLEDGMENTS

A.G., A.N., and J.-P.R. acknowledge financing from EU-H2020 IMPRESS under Grant Agreement No. 101094299. A.R. acknowledges financing from LABEX NanoSaclay and EU-H2020 ESTEEM-3 under Grant Agreement No. 823717 for doctoral funding. A.G. and X.L. also acknowledge financing from EU-H2020 ESTEEM-3 under Grant Agreement No. 823717. Nion UltraSTEM at LPS Orsay and the FIB at C2N, University of Paris-Saclay were accessed in the TEMPOS project framework (ANR 10-EQPX-0050). Z.D., B.F., and D.L. acknowledge the funding support from the Natural Science Foundation of China (No. 12174325) and Guang Dong Basic and Applied Basic Research Foundation (2023A1515011352). The work performed in Hong Kong is supported by the Research Grants Council of Hong Kong through the Early Career Scheme (CityU 21301221) and the General Research Fund (CityU 11309622, CityU 11300923). The work benefits from the framework of the joint ANR-RGC ImagingQM project (RGC, A-CityU102/23; ANR, ANR-23-CE42-0027). L.V., C.D., and M.H. acknowledge support by the Swiss National Science Foundation—division II (Grant Nos. 200020_179155 and 200020_207338) and by the European Research Council under the European Union Seventh Framework Programme (FP7/2007−2013)/ERC Grant Agreement No. 319286 (Q-MAC). A.S. acknowledges GENCI-TGCC for computing time under Grant A0130913028. We acknowledge SOLEIL Synchrotron for provision of beamtime under the proposals 20220630 and 20221574. We thank Daniele Preziosi, Alberto Zobelli, Zhizhong Li, Nicolas Jaouen, and Jean-Marc Triscone for fruitful discussions.

ABBREVIATIONS

4D-STEM,	four-dimensional scanning transmission electron microscopy
DFT	density functional theory
GPA,	geometrical phase analysis
HAADF-STEM,	high-angle annular dark-field−scanning transmission electron microscopy
HAXPES,	hard X-ray photoelectron spectroscopy
RIXS,	resonant inelastic X-ray scattering
XAS,	X-ray absorption spectroscopy

REFERENCES

(1) Dagotto, E. Complexity in strongly correlated electronic systems. *Science* **2005**, *309*, 257−262.

(2) Ahn, C.; Cavalleri, A.; Georges, A.; Ismail-Beigi, S.; Millis, A. J.; Triscone, J.-M. Designing and controlling the properties of transition metal oxide quantum materials. *Nat. Mater.* **2021**, *20*, 1462−1468.

(3) Cheong, S.-W. The exciting world of orbitals. *Nat. Mater.* **2007**, *6*, 927−928.

(4) Keimer, B.; Kivelson, S. A.; Norman, M. R.; Uchida, S.; Zaanen, J. From quantum matter to high-temperature superconductivity in copper oxides. *Nature* **2015**, *518*, 179−186.

(5) Hayward, M. Topochemical reactions of layered transition-metal oxides. *Semicond. Sci. Technol.* **2014**, *29*, 064010.

(6) Sanjaya Ranmohotti, K.; Josepha, E.; Choi, J.; Zhang, J.; Wiley, J. B. Topochemical Manipulation of Perovskites: Low-Temperature Reaction Strategies for Directing Structure and Properties. *Adv. Mater.* **2011**, *23*, 442−460.

(7) Wu, Y.; Li, D.; Wu, C.-L.; Hwang, H. Y.; Cui, Y. Electrostatic gating and intercalation in 2D materials. *Nat. Rev. Mater.* **2023**, *8*, 41−53.

(8) Li, D.; Lee, K.; Wang, B. Y.; Osada, M.; Crossley, S.; Lee, H. R.; Cui, Y.; Hikita, Y.; Hwang, H. Y. Superconductivity in an infinite-layer nickelate. *Nature* **2019**, *572*, 624−627.
(9) Zeng, S.; Tang, C. S.; Yin, X.; Li, C.; Li, M.; Huang, Z.; Hu, J.; Liu, W.; Omar, G. J.; Jani, H.; others.; et al. Phase diagram and superconducting dome of infinite-layer $Nd_{1-x}Sr_xNiO_2$ thin films. *Phys. Rev. Lett.* **2020**, *125*, 147003.
(10) Pan, G. A.; Ferenc Segedin, D.; LaBollita, H.; Song, Q.; Nica, E. M.; Goodge, B. H.; Pierce, A. T.; Doyle, S.; Novakov, S.; Córdova Carrizales, D.; others.; et al. Superconductivity in a quintuple-layer square-planar nickelate. *Nat. Mater.* **2022**, *21*, 160−164.
(11) Wei, W.; Vu, D.; Zhang, Z.; Walker, F. J.; Ahn, C. H. Superconducting $Nd_{1-x}Eu_xNiO_2$ thin films using in situ synthesis. *Sci. Adv.* **2023**, *9*, No. eadh3327.
(12) Kumah, D. P.; Disa, A. S.; Ngai, J. H.; Chen, H.; Malashevich, A.; Reiner, J. W.; Ismail-Beigi, S.; Walker, F. J.; Ahn, C. H. Tuning the structure of nickelates to achieve two-dimensional electron conduction. *Adv. Mater.* **2014**, *26*, 1935−1940.
(13) Zhang, Z.; Schwanz, D.; Narayanan, B.; Kotiuga, M.; Dura, J. A.; Cherukara, M.; Zhou, H.; Freeland, J. W.; Li, J.; Sutarto, R.; others.; et al. Perovskite nickelates as electric-field sensors in salt water. *Nature* **2018**, *553*, 68−72.
(14) Mercy, A.; Bieder, J.; Íñiguez, J.; Ghosez, P. Structurally triggered metal-insulator transition in rare-earth nickelates. *Nat. Commun.* **2017**, *8*, 1677.
(15) Zhang, H.-T.; Park, T. J.; Islam, A. N.; Tran, D. S.; Manna, S.; Wang, Q.; Mondal, S.; Yu, H.; Banik, S.; Cheng, S.; et al. Reconfigurable perovskite nickelate electronics for artificial intelligence. *Science* **2022**, *375*, 533−539.
(16) Lee, K.; Goodge, B. H.; Li, D.; Osada, M.; Wang, B. Y.; Cui, Y.; Kourkoutis, L. F.; Hwang, H. Y. Aspects of the synthesis of thin film superconducting infinite-layer nickelates. *APL Mater.* **2020**, *8*, 041107.
(17) Wu, Y.-M.; Puphal, P.; Lee, H.; Nuss, J.; Isobe, M.; Keimer, B.; Hepting, M.; Suyolcu, Y. E.; van Aken, P. A. Topotactically induced oxygen vacancy order in nickelate single crystals. *Phys. Rev. Mater.* **2023**, *7*, 053609.
(18) Osada, M.; Fujiwara, K.; Nojima, T.; Tsukazaki, A. Improvement of superconducting properties in $La_{1-x}Sr_xNiO_2$ thin films by tuning topochemical reduction temperature. *Phys. Rev. Mater.* **2023**, *7*, L051801.
(19) Subedi, A. Possible structural quantum criticality tuned by rare-earth ion substitution in infinite-layer nickelates. *Phys. Rev. Mater.* **2023**, *7*, 024801.
(20) Krieger, G.; Martinelli, L.; Zeng, S.; Chow, L. E.; Kummer, K.; Arpaia, R.; Moretti Sala, M.; Brookes, N. B.; Ariando, A.; Viart, N.; et al. others Charge and Spin Order Dichotomy in $NdNiO_2$ Driven by the Capping Layer. *Phys. Rev. Lett.* **2022**, *129*, 027002.
(21) Ren, X.; Sutarto, R.; Gao, Q.; Wang, Q.; Li, J.; Wang, Y.; Xiang, T.; Hu, J.; Zhang, F.-C.; Chang, J. Symmetry of Charge Order in Infinite-layer Nickelates. *arXiv Preprint (Condensed Matter, Superconductivity)*, 2023. arXiv:2303.02865. https://arxiv.org/abs/2303.02865 (accessed 2023-03-06).
(22) Tam, C. C.; Choi, J.; Ding, X.; Agrestini, S.; Nag, A.; Wu, M.; Huang, B.; Luo, H.; Gao, P.; García-Fernández, M.; et al. Charge density waves in infinite-layer $NdNiO_2$ nickelates. *Nat. Mater.* **2022**, *21*, 1116−1120.
(23) Rossi, M.; Osada, M.; Choi, J.; Agrestini, S.; Jost, D.; Lee, Y.; Lu, H.; Wang, B. Y.; Lee, K.; Nag, A.; et al. A broken translational symmetry state in an infinite-layer nickelate. *Nat. Phys.* **2022**, *18*, 869−873.
(24) Raji, A.; Krieger, G.; Viart, N.; Preziosi, D.; Rueff, J.; Gloter, A. Charge Distribution across Capped and Uncapped Infinite-Layer Neodymium Nickelate Thin Films. *Small* **2023**, *19*, 2304872.
(25) Parzyck, C.; Gupta, N.; Wu, Y.; Anil, V.; Bhatt, L.; Bouliane, M.; Gong, R.; Gregory, B.; Luo, A.; Sutarto, R.; et al. Absence of $3a_0$ Charge Density Wave Order in the Infinite Layer Nickelates. *arXiv preprint (Condensed Matter, Superconductivity)*, 2023. arXiv:2307.06486. https://arxiv.org/abs/2307.06486 (accessed 2023-07-12).
(26) Moriga, T.; Usaka, O.; Nakabayashi, I.; Hirashima, Y.; Kohno, T.; Kikkawa, S.; Kanamaru, F. Reduction of the perovskite-type $LnNiO_3$ (Ln = Pr, Nd) to $Ln_3Ni_3O_7$ with monovalent nickel ions. *Solid State Ionics* **1994**, *74*, 211−217.
(27) Kotiuga, M.; Zhang, Z.; Li, J.; Rodolakis, F.; Zhou, H.; Sutarto, R.; He, F.; Wang, Q.; Sun, Y.; Wang, Y.; et al. Carrier localization in perovskite nickelates from oxygen vacancies. *Proc. Natl. Acad. Sci. U. S. A.* **2019**, *116*, 21992−21997.
(28) Torriss, B.; Margot, J.; Chaker, M. Metal-insulator transition of strained $SmNiO_3$ thin films: Structural, electrical and optical properties. *Sci. Rep.* **2017**, *7*, 40915.
(29) Hÿtch, M.; Snoeck, E.; Kilaas, R. Quantitative measurement of displacement and strain fields from HREM micrographs. *Ultramicroscopy* **1998**, *74*, 131−146.
(30) Yang, C.; Wang, Y.; Sigle, W.; van Aken, P. A. Determination of Grain-Boundary Structure and Electrostatic Characteristics in a $SrTiO_3$ Bicrystal by Four-Dimensional Electron Microscopy. *Nano Lett.* **2021**, *21*, 9138−9145.
(31) Jia, Q.; Gloter, A. Real-Space Observation of Potential Reconstruction at Metallic/Insulating Oxide Interface. *Advanced Materials Interfaces* **2023**, *10*, 2202165.
(32) Kim, Y.-M.; He, J.; Biegalski, M. D.; Ambaye, H.; Lauter, V.; Christen, H. M.; Pantelides, S. T.; Pennycook, S. J.; Kalinin, S. V.; Borisevich, A. Y. Probing oxygen vacancy concentration and homogeneity in solid-oxide fuel-cell cathode materials on the subunit-cell level. *Nat. Mater.* **2012**, *11*, 888−894.
(33) Hirai, K.; Kan, D.; Aso, R.; Ichikawa, N.; Kurata, H.; Shimakawa, Y. Anisotropic in-plane lattice strain relaxation in brownmillerite $SrFeO_{2.5}$ epitaxial thin films. *J. Appl. Phys.* **2013**, *114*, 053614.
(34) Parsons, T. G.; D'Hondt, H.; Hadermann, J.; Hayward, M. A. Synthesis and structural characterization of $La_{1-x}A_xMnO_{2.5}$ (A= Ba, Sr, Ca) phases: mapping the variants of the brownmillerite structure. *Chem. Mater.* **2009**, *21*, 5527−5538.
(35) Wang, B.-X.; Zheng, H.; Krivyakina, E.; Chmaissem, O.; Lopes, P. P.; Lynn, J. W.; Gallington, L. C.; Ren, Y.; Rosenkranz, S.; Mitchell, J. F.; Phelan, D. Synthesis and characterization of bulk $Nd_{1-x}Sr_xNiO_2$ and $Nd_{1-x}Sr_xNiO_3$. *Phys. Rev. Mater.* **2020**, *4*, 084409.
(36) Wei, W.; Shin, K.; Hong, H.; Shin, Y.; Thind, A. S.; Yang, Y.; Klie, R. F.; Walker, F. J.; Ahn, C. H. Solid state reduction of nickelate thin films. *Physical Review Materials* **2023**, *7*, 013802.
(37) Krieger, G.; Raji, A.; Schlur, L.; Versini, G.; Bouillet, C.; Lenertz, M.; Robert, J.; Gloter, A.; Viart, N.; Preziosi, D. Synthesis of infinite-layer nickelates and influence of the capping-layer on magnetotransport. *J. Phys. D: Appl. Phys.* **2023**, *56*, 024003.
(38) Green, R. J.; Haverkort, M. W.; Sawatzky, G. A. Bond disproportionation and dynamical charge fluctuations in the perovskite rare-earth nickelates. *Phys. Rev. B* **2016**, *94*, 195127.
(39) Bisogni, V.; Catalano, S.; Green, R. J.; Gibert, M.; Scherwitzl, R.; Huang, Y.; Strocov, V. N.; Zubko, P.; Balandeh, S.; Triscone, J.-M.; others.; et al. Ground-state oxygen holes and the metal−insulator transition in the negative charge-transfer rare-earth nickelates. *Nat. Commun.* **2016**, *7*, 13017.
(40) Stavitski, E.; De Groot, F. M. The CTM4XAS program for EELS and XAS spectral shape analysis of transition metal L edges. *Micron* **2010**, *41*, 687−694.
(41) Ikeno, H.; de Groot, F. M.; Stavitski, E.; Tanaka, I. Multiplet calculations of $L_{2,3}$ x-ray absorption near-edge structures for 3d transition-metal compounds. *J. Phys.: Condens. Matter* **2009**, *21*, 104208.
(42) Rossi, M.; Lu, H.; Nag, A.; Li, D.; Osada, M.; Lee, K.; Wang, B. Y.; Agrestini, S.; Garcia-Fernandez, M.; Kas, J.; et al. Orbital and spin character of doped carriers in infinite-layer nickelates. *Phys. Rev. B* **2021**, *104*, L220505.
(43) Meyers, D.; Liu, J.; Freeland, J. W.; Middey, S.; Kareev, M.; Kwon, J.; Zuo, J. M.; Chuang, Y.-D.; Kim, J. W.; Ryan, P. J.; Chakhalian, J. Pure electronic metal-insulator transition at the interface of complex oxides. *Sci. Rep.* **2016**, *6*, 27934.

(44) Mikheev, E.; Hauser, A. J.; Himmetoglu, B.; Moreno, N. E.; Janotti, A.; Van de Walle, C. G.; Stemmer, S. Tuning bad metal and non-Fermi liquid behavior in a Mott material: Rare-earth nickelate thin films. *Sci. Adv.* **2015**, *1*, No. e1500797.
(45) Lee, K.; Wang, B. Y.; Osada, M.; Goodge, B. H.; Wang, T. C.; Lee, Y.; Harvey, S.; Kim, W. J.; Yu, Y.; Murthy, C.; et al. Linear-in-temperature resistivity for optimally superconducting (Nd, Sr)NiO_2. *Nature* **2023**, *619*, 288−292.
(46) Chen, L.; Zhang, Y.; Wang, X.; Jalan, B.; Chen, S.; Hou, Y. Roles of point defects in thermal transport in perovskite barium stannate. *J. Phys. Chem. C* **2018**, *122*, 11482−11490.
(47) Suntivich, J.; Gasteiger, H. A.; Yabuuchi, N.; Nakanishi, H.; Goodenough, J. B.; Shao-Horn, Y. Design principles for oxygen-reduction activity on perovskite oxide catalysts for fuel cells and metal−air batteries. *Nat. Chem.* **2011**, *3*, 546−550.
(48) Liu, Z.; Sun, L.; Huang, Z.; Li, C.; Zeng, S.; Han, K.; Lü, W.; Venkatesan, T.; Ariando, A. Dominant role of oxygen vacancies in electrical properties of unannealed $LaAlO_3/SrTiO_3$ interfaces. *J. Appl. Phys.* **2014**, *115*, 054303.
(49) Catalano, S.; Gibert, M.; Bisogni, V.; Peil, O.; He, F.; Sutarto, R.; Viret, M.; Zubko, P.; Scherwitzl, R.; Georges, A. others Electronic transitions in strained $SmNiO_3$ thin films. *APL Mater.* **2014**, *2*, 116110.
(50) Tencé, M.; Blazit, J.-D.; Li, X.; Krajnak, M.; del Busto, E. N.; Skogeby, R.; Cambou, L.; Kociak, M.; Stephan, O.; Gloter, A. Electron Energy-loss Spectroscopy Using MerlinEM-Medipix3 Detector. *Microscopy and Microanalysis* **2020**, *26*, 1940−1942.
(51) Kohn, W.; Sham, L. J. Self-consistent equations including exchange and correlation effects. *Phys. Rev.* **1965**, *140*, A1133.
(52) Giannozzi, P.; Baroni, S.; Bonini, N.; Calandra, M.; Car, R.; Cavazzoni, C.; Ceresoli, D.; Chiarotti, G. L.; Cococcioni, M.; Dabo, I.; et al. QUANTUM ESPRESSO: a modular and open-source software project for quantum simulations of materials. *J. Phys.: Condens. Matter* **2009**, *21*, 395502.
(53) Giannozzi, P; Andreussi, O; Brumme, T; Bunau, O; Buongiorno Nardelli, M; Calandra, M; Car, R; Cavazzoni, C; Ceresoli, D; Cococcioni, M; et al. Advanced capabilities for materials modelling with Quantum ESPRESSO. *J. Phys.: Condens. Matter* **2017**, *29*, 465901.
(54) Perdew, J. P.; Burke, K.; Ernzerhof, M. Generalized gradient approximation made simple. *Phys. Rev. Lett.* **1996**, *77*, 3865.
(55) Chiuzbăian, S. G.; Hague, C. F.; Avila, A.; Delaunay, R.; Jaouen, N.; Sacchi, M.; Polack, F.; Thomasset, M.; Lagarde, B.; Nicolaou, A.; et al. Design and performance of AERHA, a high acceptance high resolution soft x-ray spectrometer. *Rev. Sci. Instrum.* **2014**, *85*, 043108.
(56) Rueff, J.-P.; Ablett, J. M.; Ceolin, D.; Prieur, D.; Moreno, Th.; Baledent, V.; Lassalle-Kaiser, B.; Rault, J. E.; Simon, M.; Shukla, A. The GALAXIES Beamline at SOLEIL Synchrotron: Inelastic X-ray Scattering and Photoelectron Spectroscopy in the Hard X-ray Range. *J. Synchrotron Rad.* **2015**, *22*, 175−179.
(57) Ceolin, D.; Ablett, J.M.; Prieur, D.; Moreno, T.; Rueff, J.-P.; Marchenko, T.; Journel, L.; Guillemin, R.; Pilette, B.; Marin, T.; Simon, M. Hard X-ray photoelectron spectroscopy on the GALAXIES beamline at the SOLEIL synchrotron. *J. Electron Spectrosc. Relat. Phenom.* **2013**, *190*, 188−192.
(58) Smekal, W.; Werner, W. S.; Powell, C. J. Simulation of electron spectra for surface analysis (SESSA): a novel software tool for quantitative Auger-electron spectroscopy and X-ray photoelectron spectroscopy. *Surf. Interface Anal.* **2005**, *37*, 1059−1067.
(59) Shirley, D. A. High-resolution X-ray photoemission spectrum of the valence bands of gold. *Phys. Rev. B* **1972**, *5*, 4709.

Supporting Information for

A valence-ordered thin-film nickelate with tri-component nickel coordination prepared by topochemical reduction

Aravind Raji[1,2,9], Zhengang Dong[3,4,9], Victor Porée[2], Alaska Subedi[5], Xiaoyan Li[1], Bernat Mundet[6,7], Lucia Varbaro[6], Claribel Domínguez[6], Marios Hadjimichael[6], Bohan Feng[3,4], Alessandro Nicolaou[2], Jean-Pascal Rueff[2], Danfeng Li[3,4,⋆], and Alexandre Gloter[1,⋆]

[1]Laboratoire de Physique des Solides, CNRS, Université Paris-Saclay, Orsay, 91400, France
[2]Synchrotron SOLEIL, L'Orme des Merisiers, BP 48 St Aubin, Gif sur Yvette, 91192, France
[3]Department of Physics, City University of Hong Kong, Kowloon, Hong Kong
[4]City University of Hong Kong Shenzhen Research Institute, Shenzhen, Guangdong, 518057, China
[5]CPHT, Ecole Polytechnique, Palaiseau cedex, 91128, France
[6]Department of Quantum Matter Physics, University of Geneva, Geneva, Switzerland
[7]Electron Spectrometry and Microscopy Laboratory (LSME), Institute of Physics (IPHYS), Ecole Polytechnique Fédérale de Lausanne (EPFL), Lausanne, Switzerland
[8]LCPMR, Sorbonne Université, CNRS, Paris, 75005, France
[9]These authors contributed equally to this work
⋆Corresponding authors. Emails: danfeng.li@cityu.edu.hk, alexandre.gloter@universite-paris-saclay.fr

Contents

1 HAADF-STEM imaging in low magnification

Here we present the HAADF-STEM images of the reduced $Sm_9Ni_9O_{22}$ thin-film (Figure S1) and parent $SmNiO_3$ (Figure S2) in a lower field of view. The observed uniform out-of-plane compression in Figure S1b can be ascribed to the proper stabilization of the thin-film of the reduced phase, devoid of any defects. All the measurements including 4D-STEM were carried out at room temperature at 200 keV with a probe current of approximately 10 pA, in these conditions, the samples did not show any beam damage. Optimized parameters were used for data acquisition that involved enhancing the signal to noise ratio, without compromising the scanning speed.

1.1 $Sm_9Ni_9O_{22}$

At larger field-of-view, the GPA map of the $Sm_9Ni_9O_{22}$ have homogeneous distribution indicating the absence of defect and the formation of a new phase.

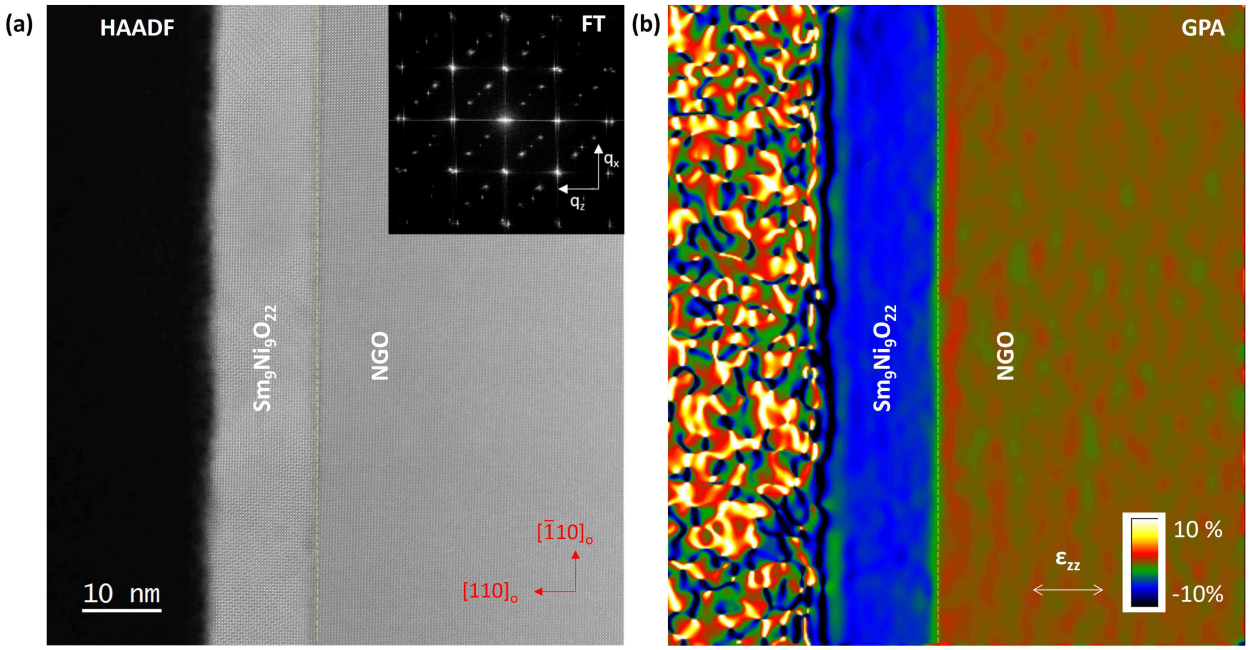

Figure S1: Structural homogeneity of $Sm_9Ni_9O_{22}$ thin-film. (a) Low magnification HAADF image of the $Sm_9Ni_9O_{22}$ thin-film, viewed along the $[010]_{pc}$ zone axis. A Fourier transform is shown in the inset. (b) The corresponding out-of-plane strain map by GPA. A uniform compression of 7% for the o-o-p parameter is observed for the whole $Sm_9Ni_9O_{22}$ thin-film (the substrate o-o-p is the reference), indicating the homogeneity of the thin-film.

1.2 $SmNiO_3$

The bulk SNO possesses an orthorhombic Pbnm structure and lattice parameters a_o = 5.328Å, b_o = 5.437Å and c_o = 7.567Å. The SNO unit cell can be described by a pseudo-cubic unit with a_{pc} = 3.799Å. The NGO substrate has a_o = 5.433Å, b_o = 5.503Å, and c_o = 7.716Å when also expressed within Pbnm orthorhombic space group. The SNO thin film and substrate have structural continuity and thus similar crystallographic orientations when observed in STEM. Due to the substrate strain, the GPA derived pseudo-cubic out-of-plane value of SNO is 3.78Å.

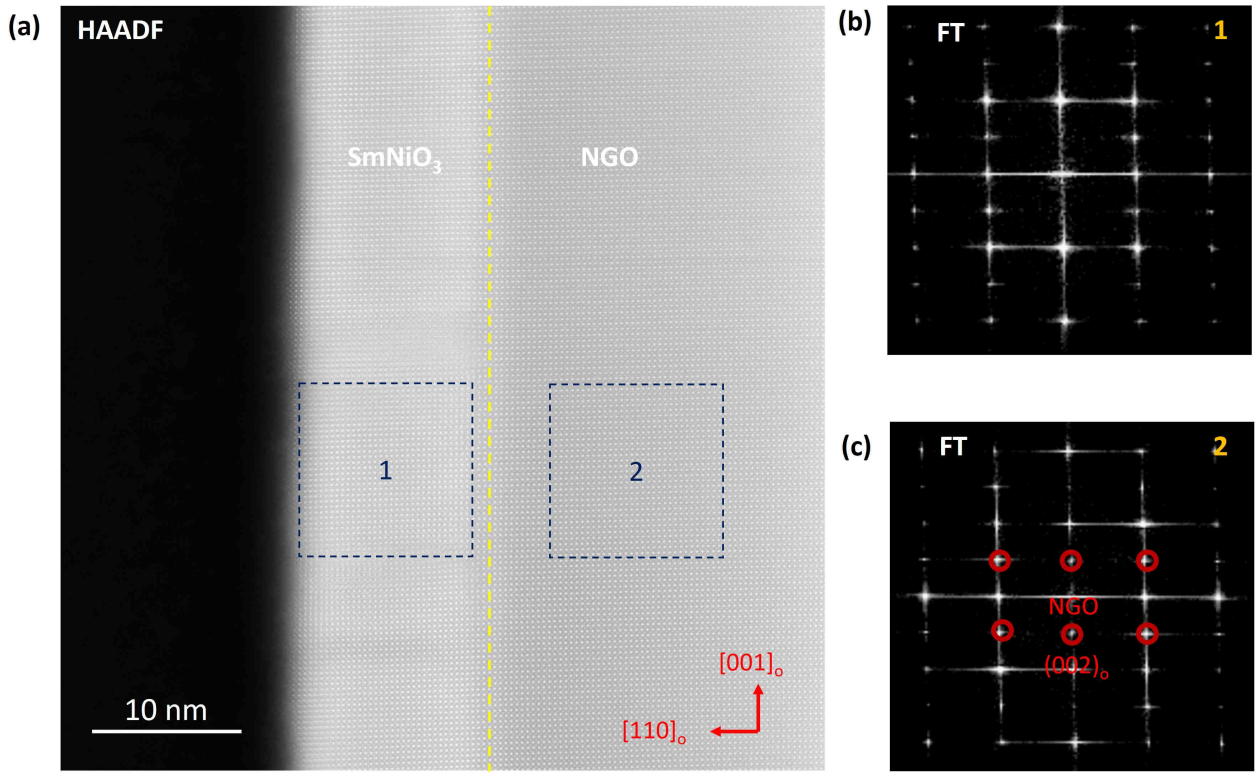

Figure S2: The Orthorhombic $SmNiO_3$ thin-film. (a) A low magnification HAADF image of $SmNiO_3$ thin film on the orthorhombic $NdGaO_3$ substrate with in-plane $[001]_o$ axis. (b & c) The Fourier Transform on (b) $SmNiO_3$ and (c) Substrate $NdGaO_3$.

2 Building the new phase with oxygen vacancies

2.1 Structural family of $A_nB_nO_{3n-1}$ formed by $(n0n)_{pc}$ oxygen vacancies plane

The Figures S3(a-f) show the positions of the columns of removed apical oxygens to form the $A_nB_nO_{3n-1}$ structure for n = 1 to n = 6 along with the corresponding stoichiometries. For the general case, the new structural family of $A_nB_nO_{3n-1}$ is thus formed by $(n0n)_{pc}$ oxygen vacancy planes starting on a cubic perovskite ABO_3. Such structures have then been relaxed by ab-initio either constraining or not the a,b axis to the substrate. The Figures S3g shows the resulting relaxed c-axis parameters in the case of $Nd_nNi_nO_{3n-1}$ with and without the constrain by a $SrTiO_3$ substrate. This corresponds to the case of the most reported infinite-layer nickelate obtained by topotactic reduction, id est, the case of $NdNiO_2$ // $SrTiO_3$. The Figure S3h reports the resulting relaxed c-axis parameters in the case of $Sm_nNi_nO_{3n-1}$, free and constrained by substrate $NdGaO_3$, corresponding to the studied system in the main text. As expected, the c-axis parameters increase with the oxygen content ($A_nB_nO_{3n-1}$) from the IL-nickelate (n = 1) toward the parent perovskite that would be for n = ∞. In the case of $Nd_nNi_nO_{3n-1}$, the c-axis parameter is around 3.65Å for n = 3, and it converges to about 3.75Å for n higher than 4 when it is not constrained. The constrain by the substrate result in overall shorter out-of-plane axis. Similar trends is obtained for the $Sm_nNi_nO_{3n-1}$ with shorter c-axis parameters as expected due to the difference of Rare-Earth size.

Figure S4 shows the relaxed atomic structures of the $Sm_nNi_nO_{3n-1}$ family for n = 1 to 4. The n = 1 case corresponds to that of an infinite-layer nickelate, with c = 3.22 Å. On observing the HAADF and 4D-STEM images along in-plane pseudo-cubic axis (the 0° or 90° projection mentioned in the main text), the experimental $Sm_9Ni_9O_{22}$ have a rather identical structure as the $A_3B_3O_8$ in Figure S4c (the n = 3 member). After relaxation, a short and a long distances in-between Sm columns appear with respectively $\approx$ 3.60 Å and $\approx$ 4.30 Å . The presence of a Sm doublet (for 1/3 of the Sm columns) is noticeable and is also in agreement with the STEM observation. Similar kind of reconstructions are visible for the n = 4 member, but for instance, with more Sm doublets (*i.e.* for 1/2 of the Sm columns).

2.2 $A_9B_9O_{22}$ from intricating $\{303\}_{pc}$ Vo planes

In this section, we now focus on the cases where the oxygen deficient structures having a triple periodicity with respect to the cubic perovskite and discuss the corresponding Ni coordinations.

At first, we report in Figure S5a, the already proposed $A_3B_3O_7$ structure [1] which is resulting from removing oxygen from the apical sites on only one projection. The Ni sites is then existing in square-planar and octahedral coordinations with the oxygen atoms. Such a structure is very different from the STEM observation and spectroscopic observations.

In Figure S5b, the $A_3B_3O_8$ structure is resulting from removing oxygen from the apical sites with a (303)pc periodicity on one projection as discussed in the previous section. This results in Ni sites existing in pyramidal and octahedral coordinations with the oxygen atoms.

We then consider the case where several $\{303\}_{\text{pc}}$ oxygen vacancies planes are simultaneously removed since the experimental STEM data have demonstrated that $(303)_{pc}$ and $(033)_{pc}$ oxygen vacancy planes are coexisting in the experimental structure. Removing oxygen from the apical sites with a $(303)_{pc}$ and $(033)_{pc}$ periodicity (*i.e.* along two orthogonal projections) give the more oxygen reduced structure showed in Figure S5(c). It corresponds to $A_3B_3O_{7.33}$ ($A_9B_9O_{22}$) stoichiometry. There, the Ni sites are existing in pyramidal, square-planar and octahedral coordinations with the oxygen atoms.

It can be compared with the the $A_3B_3O_8$ structure where removing oxygen from the apical (out-of-plane) sites with a $(303)_{pc}$ periodicity on one projection is now combined by removing the equatorial (in-plane) sites with $(033)_{pc}$ planes peridocity on the other orthogonal projection (Figure S5d). This results in Ni sites existing in pyramidal, and octahedral coordinations with the oxygen atoms.

It is interesting to note that theses structures encompass Ni being in octahedral, tetrahedral, pyramidal and square-planar coordinations with the neighbouring oxygen atoms with complex distributions. Among them, only the $A_9B_9O_{22}$ phase has Ni sites in octahedral, pyramidal **and square-planar** coordinations as shown in Figure S5c, thereby suggesting the possible route toward the formation of IL-nickelate, where all Ni sites are in square-planar coordination with oxygen. The occurrence of square-planar coordination comes from the removal of apical oxygen planes over two different directions.

Having demonstrated these for a 3x3x3 supercell of a cubic perovskite, a more general relaxation of the $Sm_9Ni_9O_{22}$ phase is carried out starting from a 6x6x6-supercell (such 6x6x6 supercell before removing the oxygen atoms had 1080 atoms). This is shown in Figure S6. Beginning with a 6x6x6-cubic supercell of $SmNiO_3$, the $(303)_{\text{pc}}$ and $(033)_{\text{pc}}$ families of apical oxygen were removed (Figure S6a-b). The crystal was allowed to relax minimizing the total force under substrate constrain. The relaxation give a reduced c-axis parameter to 3.63 Å that is rather comparable to the c-axis of the $A_3B_3O_8$ structure where only one $(303)_{\text{pc}}$ families of apical oxygen was removed. This is also in fair agreement with the experimental values. The resulting 960-atom tetragonal structure is shown in different orientations (Figure S6d-f) and is comparable to the STEM experiments (e.g., the observation of long and short Sm-Sm distances o 4.10Å and 3.60Å along two perpendicular orientations). This structure was then reduced to a smaller primitive monoclinic unit cell using symmetry. The structural parameters of this monoclinic structure is given in Table S1. It is to note that, from the symmetry, one can go back to the 960-atom tetragonal structure with the lattice vectors $\vec{a_T},\ \vec{b_T},\ \vec{c_T}$ expressed in the symmetrized monoclinic parameters $(\vec{a_m},\ \vec{b_m},\ \vec{c_m})$ by : $\vec{a_T} = \vec{a_m} + \vec{b_m} + 2\vec{c_m},\ \vec{b_T} = \vec{a_m} - \vec{b_m} + 2\vec{c_m},\ \vec{c_T} = 2\vec{a_m} - 2\vec{c_m}$.

This work clearly evidences that a new phase can be created by intricating $\{303\}_{pc}$ Vo planes. This $A_9B_9O_{22}$ phase could be a member of a potentially new family of nickel oxides, that forms by intricating $\{\text{n0n}\}_{\text{pc}}$ ordered Vo. Overlapping $(\text{n0n})_{\text{pc}}$ and $(\text{0nn})_{\text{pc}}$ apical oxygen vacancy planes results in a general formula $A_{n^2}B_{n^2}O_{3n^2-2n+1}$. It is indeed spanning from the IL-ABO_2 with only square planar to the perovskite ABO_3 with only octahedral Ni sites. In-between, octahedral, square-planar and pyramidal sites are in the ratio $(n-2)^2 : 2 : (4n-6)$. Such $\{\text{n0n}\}_{\text{pc}}$ planes could be seen as an analogous case of the Ruddlesden-Popper (RP) faults that is also present from the individual 2D defects and can scale to form fully developed RP phase.

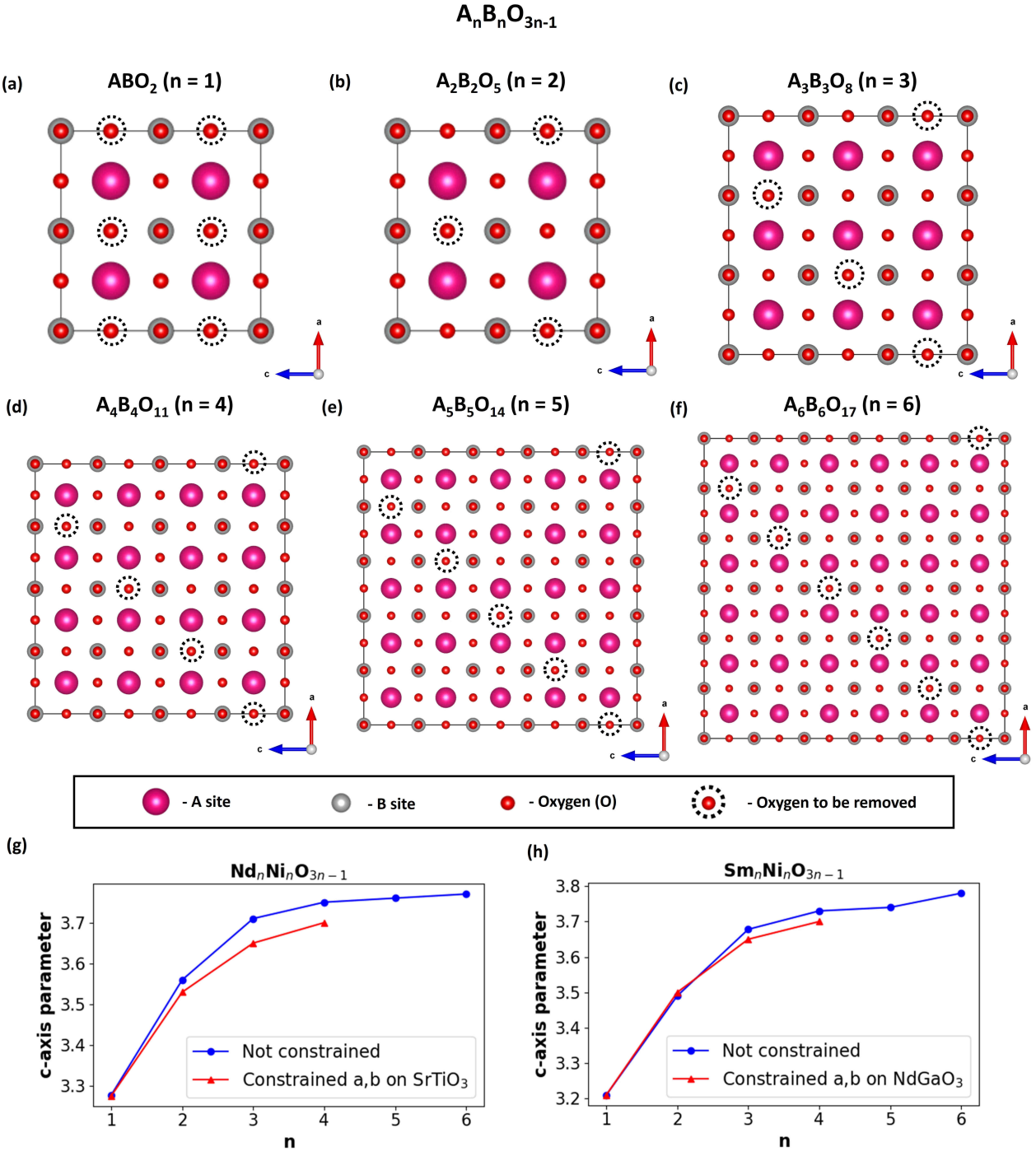

Figure S3: $A_nB_nO_{3n-1}$ family with the oxygen vacancies to be induced for (a-f) n = 1 - 6. (g,h) The corresponding c-axis parameters obtained by atomic relaxation for different n, with an without constraining in plane parameters on the substrate for a (g) $Nd_nNi_nO_{3n-1}$//$SrTiO_3$ system and (h) $Sm_nNi_nO_{3n-1}$//$NdGaO_3$ system. As it is evident, the c-axis parameters increases with the oxygen content ($A_nNi_nO_{3n-1}$). IL-nickelate corresponds to n = 1, while the parent perovskite would be for n = ∞. Furthermore constraining the in-plane parameters ($NdGaO_3$: $a = 3.86$ Å, $b = 3.86$ Å and $SrTiO_3$: $a = b = 3.91$ Å) with these substrates reduces the c-axis parameter upon crystal relaxation, for n higher than 2.

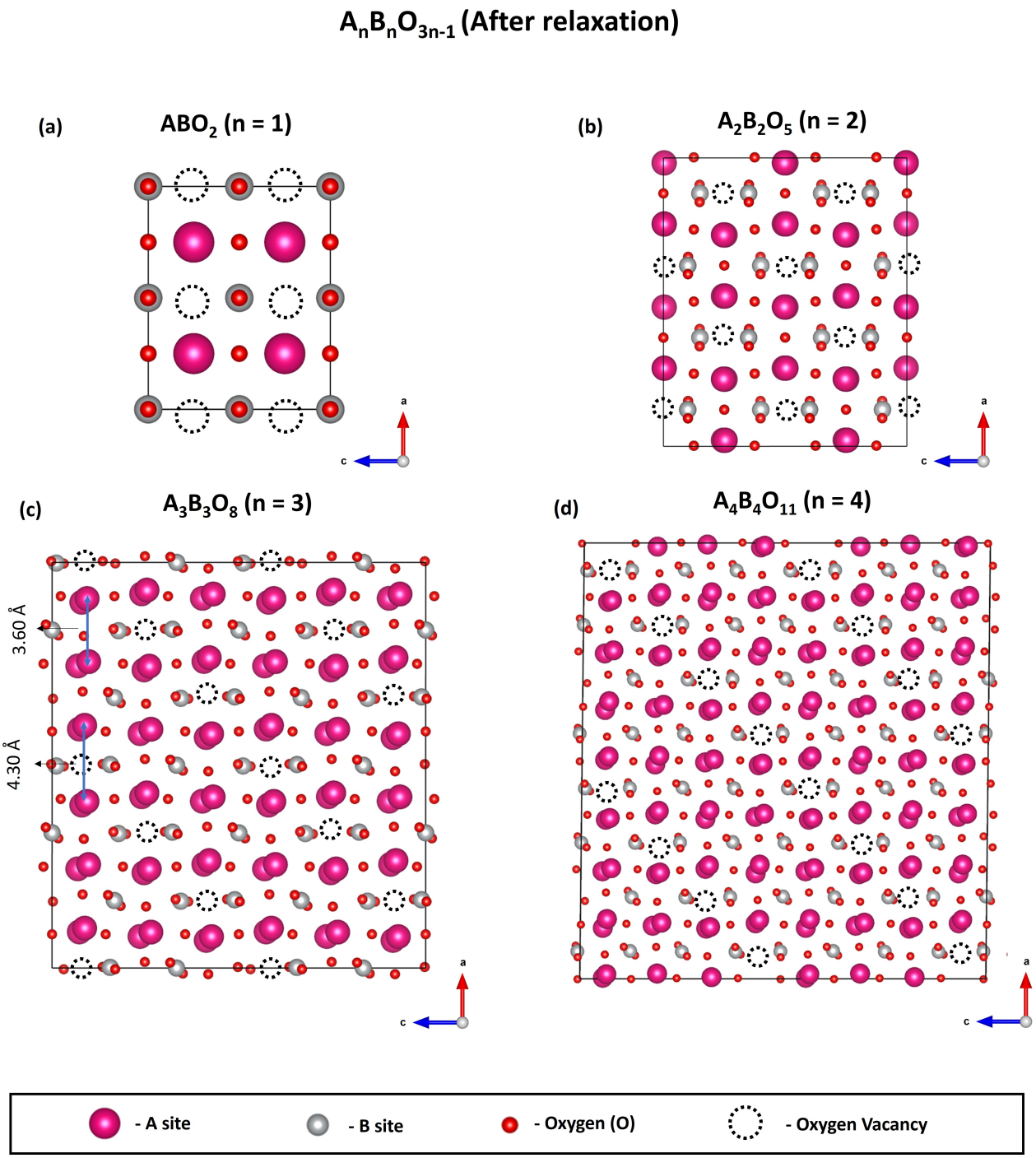

Figure S4: Relaxed structures of the $Sm_nNi_nO_{3n-1}$ family with the oxygen vacancies (a-d) n = 1 - 4.

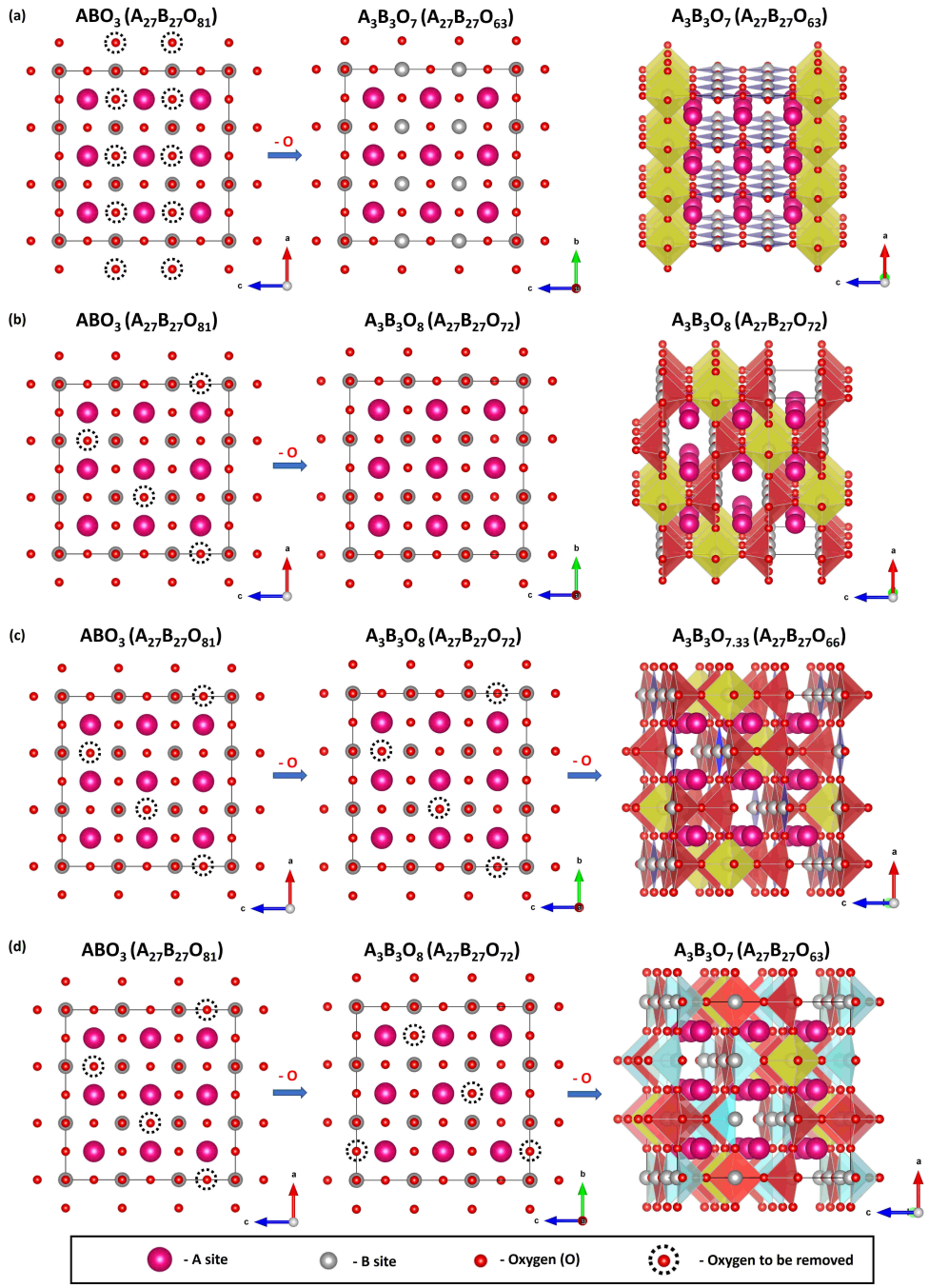

Figure S5: Different structures resulting by 1/3 removal of oxygen along various directions from a parent ABO_3 cubic 3x3x3 supercell. (a) The $A_3B_3O_7$ structure resulting from removing oxygen from the apical sites on one projection as shown. It results in Ni sites existing in square-planar and octahedral coordinations with the oxygen atoms. (b) The $A_3B_3O_8$ structure resulting from removing oxygen from the apical sites with a $(303)_{pc}$ periodicity on one projection. This results in Ni sites existing in pyramidal and octahedral coordinations with the oxygen atoms. (c) The $A_3B_3O_{7.33}$ ($A_9B_9O_{22}$) structure resulting from removing oxygen from the apical sites with a $(303)_{pc}$ and $(033)_{pc}$ periodicity. This results in Ni sites existing in pyramidal, square-planar and octahedral coordinations with the oxygen atoms. (d) The $A_3B_3O_7$ structure resulting from removing oxygen from the apical (out-of-plane) sites with a $(303)_{pc}$ periodicity on one projection and equatorial (in-plane) sites with the same periodicity along the other orthogonal projection. This results in Ni sites existing in pyramidal, tetrahedral and octahedral coordinations with the oxygen atoms.

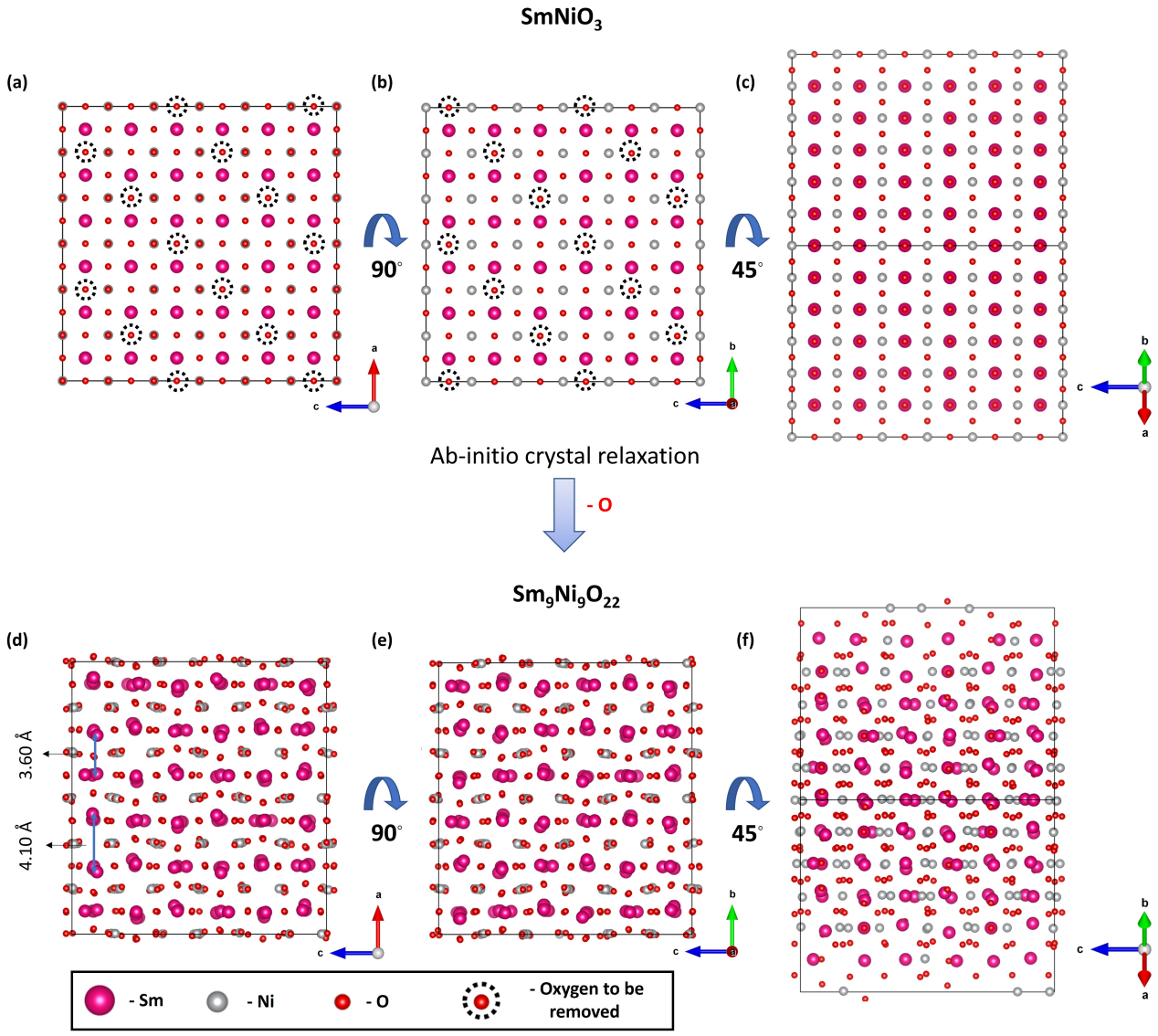

Figure S6: Ab-initio crystal structure relaxation of a 6x6x6 cubic supercell of $SmNiO_3$ with $(303)_{pc}$ and $(033)_{pc}$ oxygen vacancies, resulting in the $SmNiO_{2.44}$ ($Sm_9Ni_9O_{22}$) structure. (a-c) The intial 6x6x6 supercell of cubic $SmNiO_3$ ($a = 3.79$ Å), along the (a) 0°, (b) 90°, and (c) 135° projections. Note that the oxygen vacancies to be induced are indicated in (a) and (b), but they are not indicated along the 135° projection in (c) due to overlap with other oxygen atoms. (d-f) The relaxed tetragonal structure along the (a) 0°, (b) 90°, and (c) 135° projections. The in-plane parameters ($a = b = 3.79$ Å) are kept the same, while the out-of-plane parameter is reduced ($c = 3.63$ Å).

C2/m	$a = 9.02$Å	$b = 16.09$Å	$c = 6.47$Å
(12)	$\alpha = 90.00°$	$\beta = 87.57°$	$\gamma = 90.00°$
Atom	**x**	**y**	**z**
Ni1	0.13629	0.00000	-0.12659
Ni2	-0.50000	0.00000	0.50000
Ni3	0.31121	-0.16600	0.19587
Ni4	0.00000	-0.16814	0.50000
Sm1	0.00000	-0.18474	0.00000
Sm2	-0.31539	-0.15216	0.29485
Sm3	0.34038	-0.50000	0.64052
Sm4	0.00000	-0.50000	1.00000
O1	0.09218	-0.08261	-0.33878
O2	-0.18560	-0.08740	-0.06043
O3	-0.63850	-0.08647	0.39467
O4	0.25000	-0.25000	0.00000
O5	-0.09169	-0.24204	0.31874
O6	-0.36078	0.00000	0.27300
O7	-0.50000	-0.14450	1.00000

Table S1: The structural parameters of the $Sm_9Ni_9O_{22}$ monoclinic $C2/m$ unit cell, reduced using symmetry from the relaxed 6x6x6 supercell. All the sites have an occupancy of 1.

3 Complementary Spectroscopic analysis of $SmNiO_3$ and $Sm_9Ni_9O_{22}$

Here we present temperature dependent XAS, RIXS measurements carried out on $SmNiO_3$ at the Ni-L and O-K edges. We also present RIXS measurements in $Sm_9Ni_9O_{22}$ in more details. This forms a comparative analysis between the well studied perovskite ABO_3 and the novel phase $A_9B_9O_{22}$.

3.1 The metal-to-insulator transition of $SmNiO_3$

As shown in Figure S7, the XAS and RIXS measurements with a linearly polarizerd light on $SmNiO_3$ at the Ni-L edge shows no strong dichroism, representative of symmetry of the octahedral NiO_6 coordination in this system. For instance, the XAS Ni-L3 spectra are similar for both polarisations in the total electron yield at 25K (Figure S7f), and they shows strong differences when compared to those at 300K (Figure S7g), indicating an electronic transition towards a more metallic state. Such a difference is similar to what discussed in Bisogni et al. [2] for $NdNiO_3$. In the RIXS signatures in Figure S7(b-e), the Ni dd-transition at around 1.3 eV shows a blue shift towards a higher energy loss with temperature, further indicating this metallic transition. Although the MIT of $SmNiO_3$ is at 375K, as evidenced by transport measurements, some regions of the thin-film near the surface can undergo a metallic transitions at a lower temperature. This is being reflected in our spectroscopic signatures at room temperature, and similar findings were also reported before [2].

The electronic transition evidenced from the Ni-L edge spectra is expected to give some spectroscopic signatures in the O-K edge. Here we discuss the O-K XAS and RIXS measurements on $SmNiO_3$ (Figures S9 and S10). A difference in the XAS spectra is observed for the O-K edge pre-peak, when going from 25K to 300K (Fig S9a and S9d). The pre-peak intensity at ca. 525.5 eV appear with lower intensity at room temperature. Furthermore, by overlapping the O-K pre-peak measured at both temperatures and normalizing their intensities as shown in Figure S10(j), the width of the pre-edge is also seen as narrower at lower temperature (25K) and a blue shift can also be observed (e.g., on the slope). This can be a possible representation of the spectroscopic nature of the MIT at the O-K edge. From a Ni-O hybridization model, the octahedral sites in the metallic regime of the perovskite nickelate [2, 3] are in a Ni $3d^8\underline{L}$ configuration with O-2p hole rich ground state. Such negative charge-transfer picture is at the origin of the strong pre-peak at the O-K edge. At lower temperature, the ground state has been described as altered, with two electron configurations, one for an expanded $3d^8$ Ni site and another one for a collapsed $3d^8\underline{L}^2$ Ni site. The reinforcement of the pre-edge intensity along with its narrowing might be relevant to this latest electron configuration. The small blue-shift of the O-K pre-edge can also be viewed in accordance with a band gap opening as expected from the MIT-like transition observed from the Ni-L edge at low temperature.

Corresponding RIXS O-K data have also been measured at both temperatures. They are represented in maps with the energy-loss as a function of the photon energy in Figure S9. They are also represented in a photon-in and photon-out maps in Figure S10. The narrower and stronger intensity of the pre-edges at low temperature, is now even more visible when looking at the energy-loss at ca. 525.5 eV in Figure S9. In Figure S10i, a very clear blue shift is measured at low temperature for the RIXS energy-loss profiles associated to the O-K pre-peak incoming photon energy, certainly in relation with a partial band-gap opening.

3.2 Temperature dependent electronic transitions in $Sm_9Ni_9O_{22}$

The XAS TEY spectra of $Sm_9Ni_9O_{22}$ at 300K is shown in Figure S7h, and it does not show a strong difference compared to the measurements at 25K as discussed in the main text. This can be attributed to a rather stability in the population for configurations associated with primary ionic electron configuration (Ni^{1+} and Ni^{2+}) as a function of temperature. Further investigation of this with respect to the Ni-L RIXS profiles is shown in Figure S8. Here, on comparing Figure S8 a and c, the dd-like transitions at around 0.8 eV, is having a small shift of around 0.2 eV to a higher energy loss at 25K. Considering the electronic picture from $SmNiO_3$, where RIXS signatures were obviously showing more sensitivity

to small electronic change as compared to XAS, this can be an indication of some small evolution in the $Sm_9Ni_9O_{22}$ ground state at low temperature pertaining to the Ni-d orbital.

Interestingly, the O-K XAS edge was already showing variations between room and low-temperatures, as discussed in the main text. Specifically, the pre-peak in the O-K XAS shows a blurring at room temperature. Furthermore, there was a strong dichroic nature for these O-K prepeaks. As in the main text, Figure 5, the O-K XAS pre-edge in this system shows polarization dependent over the three peaks. They are stronger at energies 527.2 eV for a σ polarization, then at 527.6 eV for a π polarization and at 528.9 eV for a σ polarization. Some additional presentation of the RIXS spectra measured at the O-K is given in Figure S11 (maps) and S12 (profiles). Interestingly, on comparison with the RIXS map in Figure S11, we can interpret that these 3 peaks stay rather similar with temperature, although accompanied by a fluorescence line at a low energy loss that is appearing only at room temperature. This can also be seen in Figure S12, where the temperature dependant RIXS line profiles at resonance energies of 527.6 eV, 528.4 eV, and 528.9 eV are given. The peak representative of the fluorescence line emerges at 300K, and exists at the three incident energies. As discussed in the main text, the pre-peaks and their dichroic behavior can be compared with the density of states in Figure S16. They are the signature of the O-2p orbitals hybridized with the unoccupied $3d_{x^2-y^2}$ of the Ni^{1+} and $3d_{z^2}$ of the Ni^{2+}. Typically, the Ni^{2+} are the most populated sites giving birth to O-K pre-edge despite their rather ionic character.

The strong temperature difference is for a non-dichroic fluorescence line. It might concern the Ni^{3+} in octahedra. Indeed, by analogy of the peroskite nickelate, such valence is more prone to imply charge transfer configuration. Despite the small amount of such octahedral Ni^{3+} at room temperature, they thus might give a substantial spectral weight in the pre-edge. The subsequent disappearance of it at a low temperature points to the localization of these charge in the octahedral sites. Instead of the charge fluctuation of the perovskite parent phase, $3d^8\underline{L} \longleftrightarrow 3d^8$ + $3d^8\underline{L}^2$, the isolated Ni^{3+} of the$Sm_9Ni_9O_{22}$ might have different one with temperature (e.g. $3d^8\underline{L} \longleftrightarrow 3d^7$ more in accordance with the RIXS spectroscopic observation) .

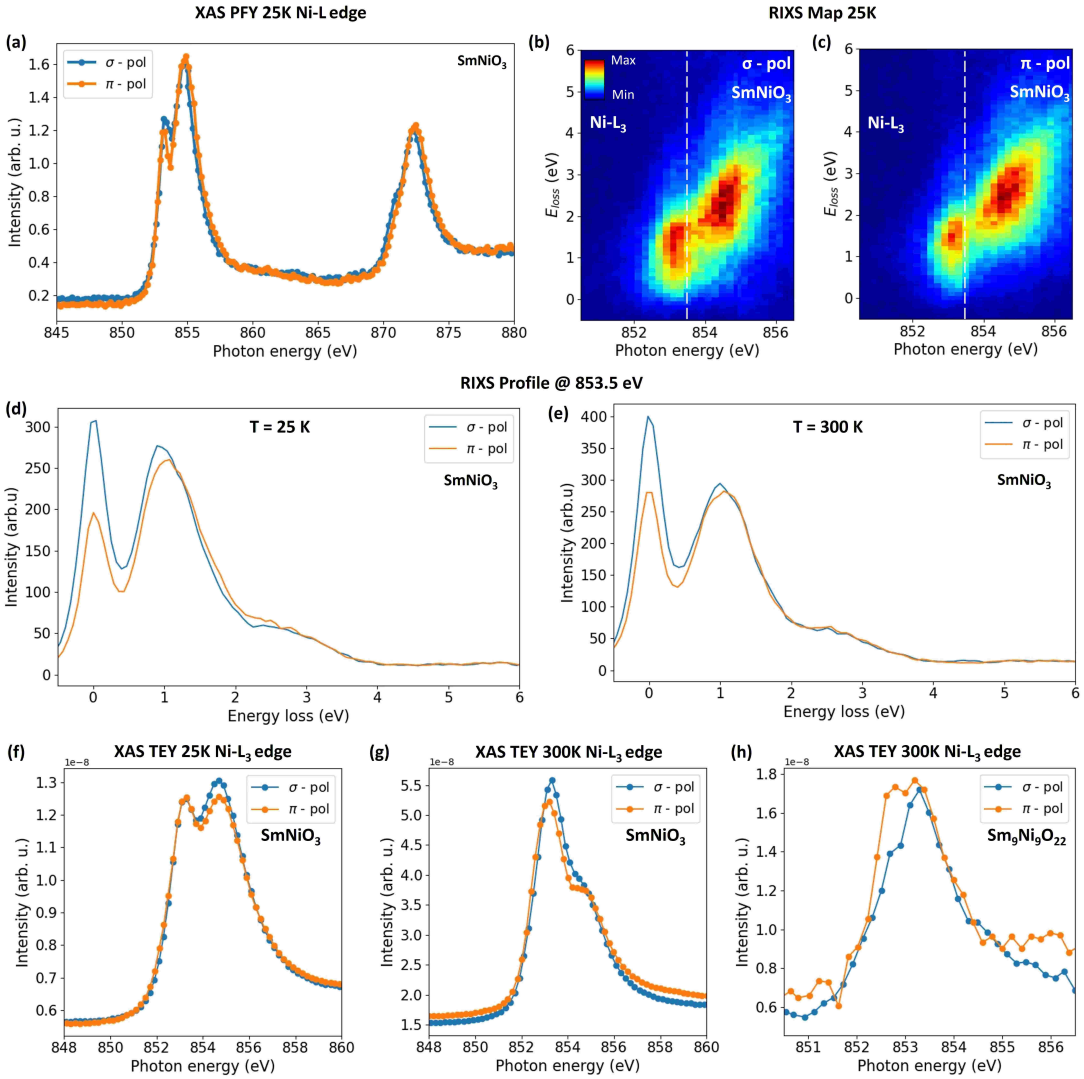

Figure S7: RIXS and XAS of $SmNiO_3$ and $Sm_9Ni_9O_{22}$. (a) Partial fluorescence yield (PFY) XAS spectra at Ni - L edge of $SmNiO_3$ in two incident photon polarizations at 25K. (b & c) The corresponding RIXS maps at Ni - L_3 of $SmNiO_3$ in (b) σ polarization and (c) π polarization. (d & e) Temperature dependent variations in RIXS XLD profile from both polarizations in $SmNiO_3$ at 853.5 eV for (d) T = 25 K and (e) T = 300 K. (f & g) Total electron yield (TEY) XAS spectra at Ni - L_3 edge of $SmNiO_3$ for two incident polarizations at (f) T = 25 K and (g) T = 300 K. (f) TEY XAS spectra at Ni - L_3 edge of $Sm_9Ni_9O_{22}$ for two incident polarizations at 300 K. The XAS spectra in PFY and TEY mode are identical, as depicted here for $SmNiO_3$. The TEY spectra of $SmNiO_3$ at 300K and 25K shows the metal-to-insulator transition, while the spectra of $Sm_9Ni_9O_{22}$ stays the same at 25K and 300K. Only TEY of the Ni-L are probed at 25K and 300K but they are very similar as the one reported by Bisogni et al. [2] showing that part of the thin film, certainly close to the surface is entering in the MIT coexistence. At RT, indeed the peak separation is getting smaller, and the width is changing very similarly as what they report by TEY in the case of $NdNiO_3$. RIXS probes more bulk and hence shows weaker differences. Nevertheless, a small shift to higher energy is seen at $\approx$ 1 eV energy loss measured at an excitation energy of 853.5 eV. It shows, at least, a partial charge disproportion when compared to the RIXS reported by Bisogni et al. [2].

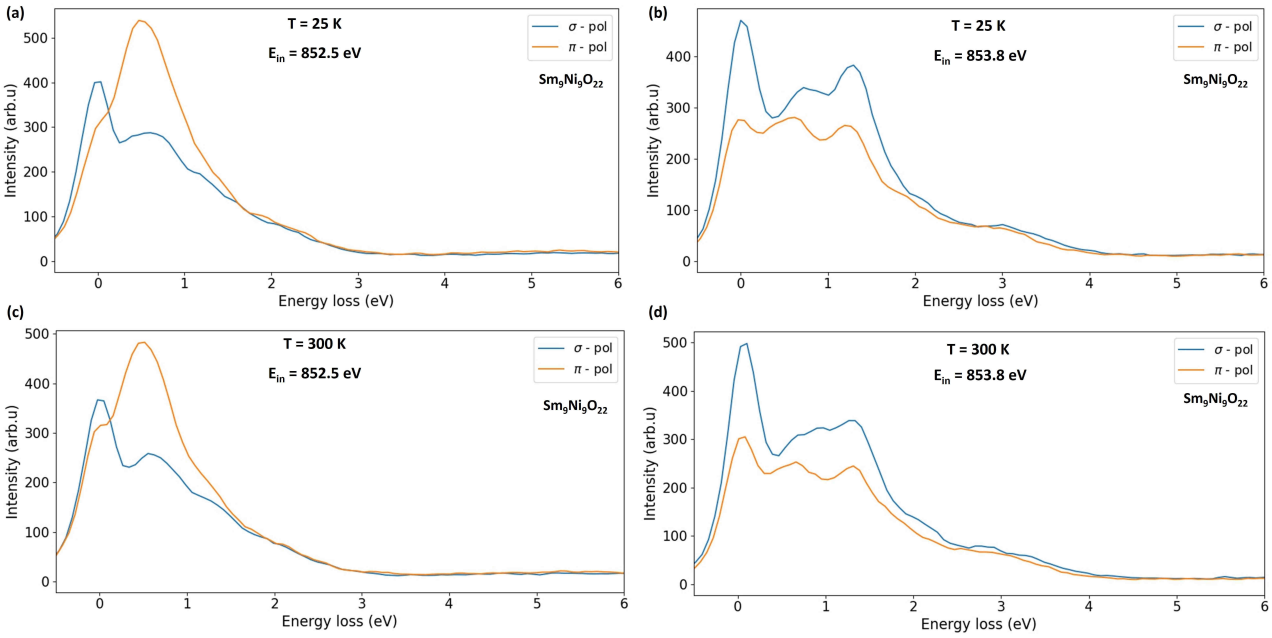

Figure S8: Temperature dependant RIXS line Profile of $Sm_9Ni_9O_{22}$ at different photon energies. (a & b) The measurements at 25K, for a photon energy of (a) 852.5 eV and (b) 853.8 eV. (c & d) The measurements at 300K, for a photon energy of (c) 852.5 eV and (d) 853.8 eV.

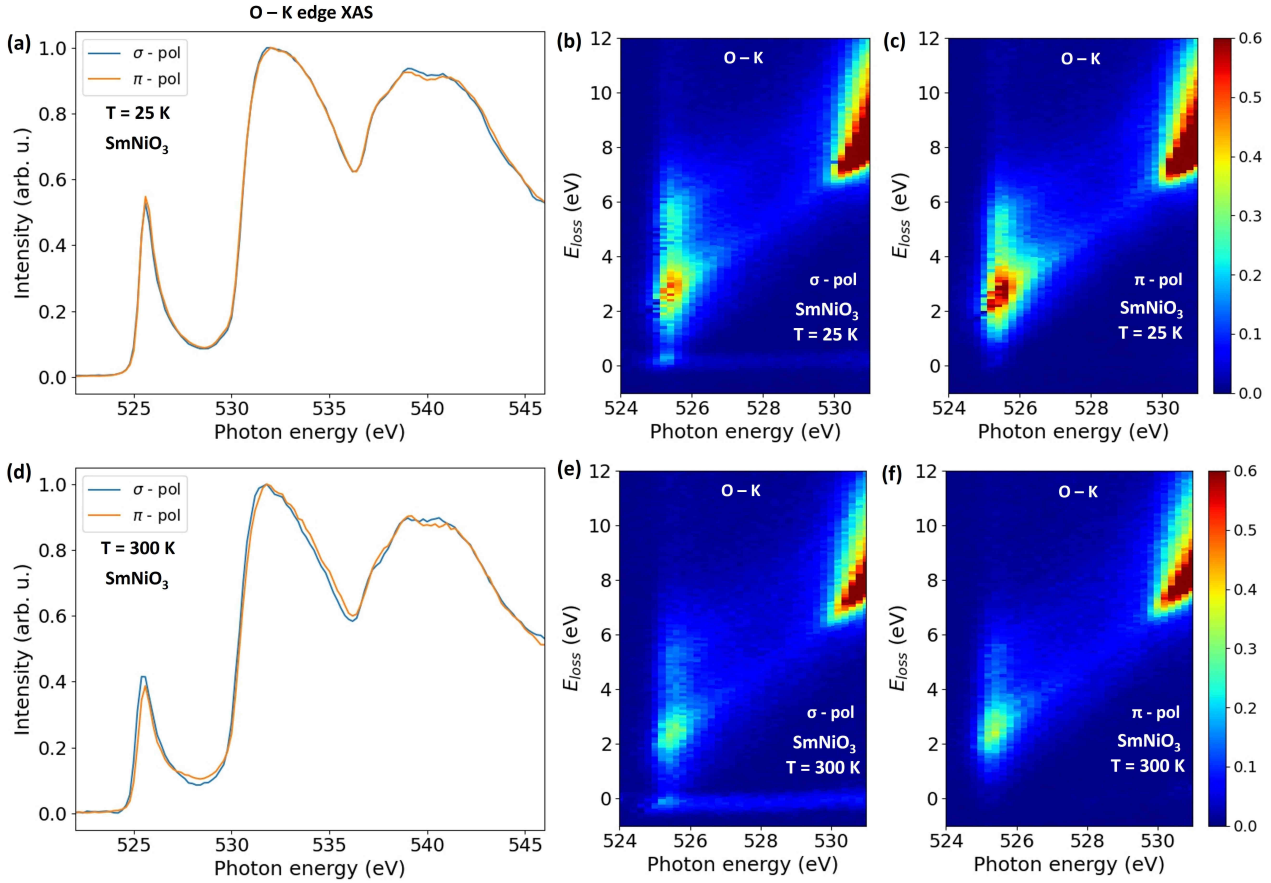

Figure S9: Temperature dependent spectroscopic studies at the O-K edge by XAS and RIXS (in energy loss scale) of $SmNiO_3$. (a-c) Measurements at T = 25 K, (a) O-K edge PFY XAS spectra in σ and π incident polarizations, (b & c) RIXS map at O-K edge for (b) σ incident photon polarization and (c) π incident photon polarization. (d-f) Measurements at T = 300 K, (d) O-K edge PFY XAS spectra in σ and π incident polarizations, (e & f) RIXS map at O-K edge for (e) σ incident photon polarization and (f) π incident photon polarization.Notably, as seen in XAS and made even clearer in the RIXS maps, the energy width of the O-K pre-edge is getting narrower and is shifted to a higher absorption energy at low temperature. Similar narrowing at the XAS pre-edges was reported for a nickelate metal-to-insulator transition (MIT) [3], confirming that some domains have a metallic character at RT. As expected, the parent structure has a weak dichroism for its spectral signatures, including the Raman-like energy losses observed at an excitation energy corresponding to the O-K pre-edge. In this pre-edge region, RIXS maps also evidence low-energy loss features (less than 0.5 eV) only at RT, in a rather similar way that was reported with low-energy electron-hole pair continuum at the Ni-L edge RIXS for a metallic nickelate [2].

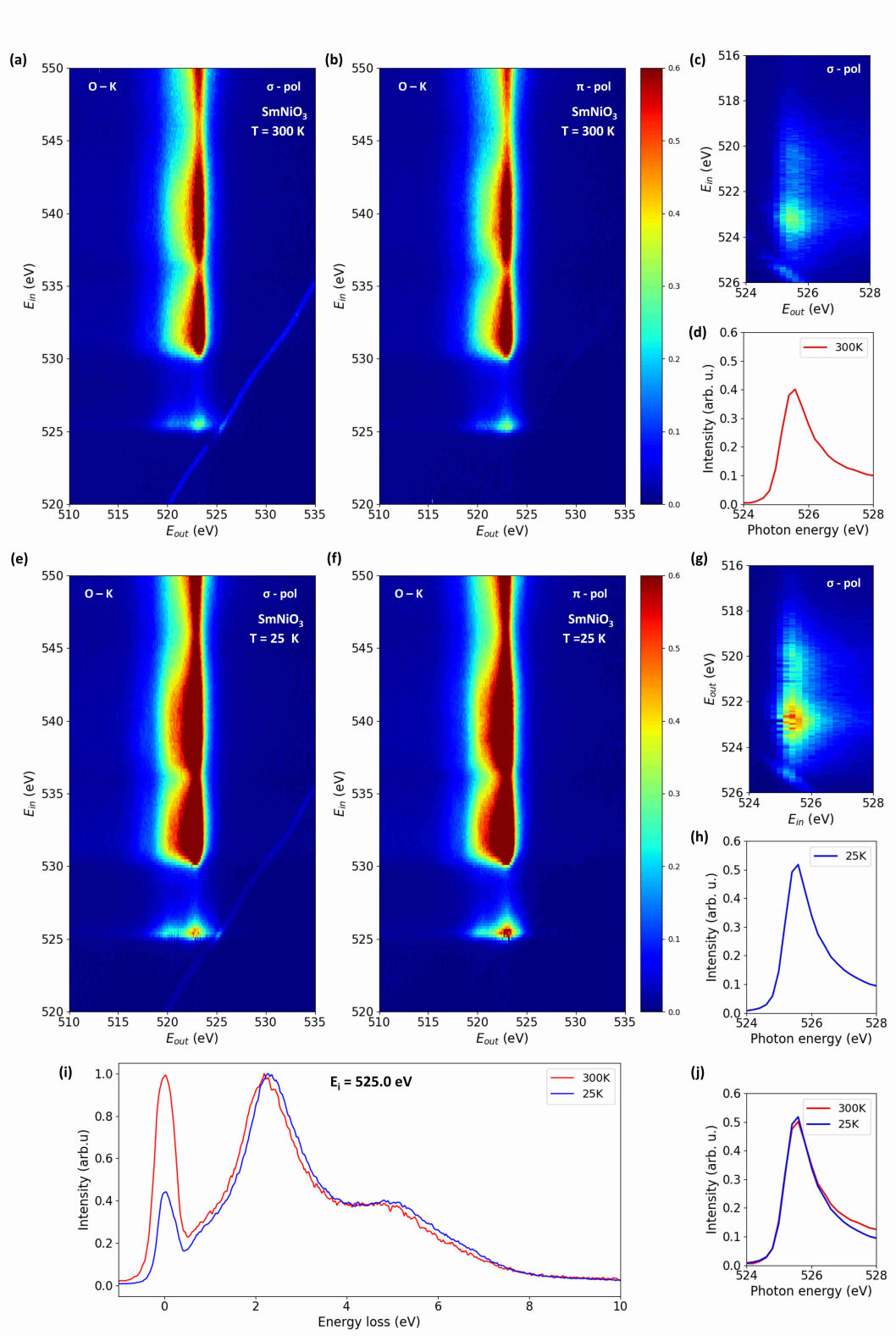

Figure S10: RIXS Map and XAS of O-K edge of $SmNiO_3$ showing a temperature dependent electronic transition. (a-d) Measurements at 300K. (a,b) RIXS map in incident (E_{in}) and detected (E_{out}) photon energy scales for (a) σ and (b) π incident photon polarisations, (c) A magnified RIXS map of a selected region in (a), (d) The XAS PFY plot of the O-K pre-edge, combining both polarisations. (e-h) Measurements at 25K. (e,f) RIXS map in incident (E_{in}) and detected (E_{out}) photon energy scales for (e) σ and (f) π incident photon polarisations, (g) A magnified RIXS map of a selected region in (e), (h) The XAS PFY plot of the O-K pre-edge, combining both polarisations. (i) Comparing the RIXS line profile at an incident photon energy of 525.0 eV for temperatures 300K and 25K, showing a blue shift at 25K. (j) The normalized-maxima-aligned pre-edge of O-K, for both temperatures. It shows a wider pre-edge at 300K.

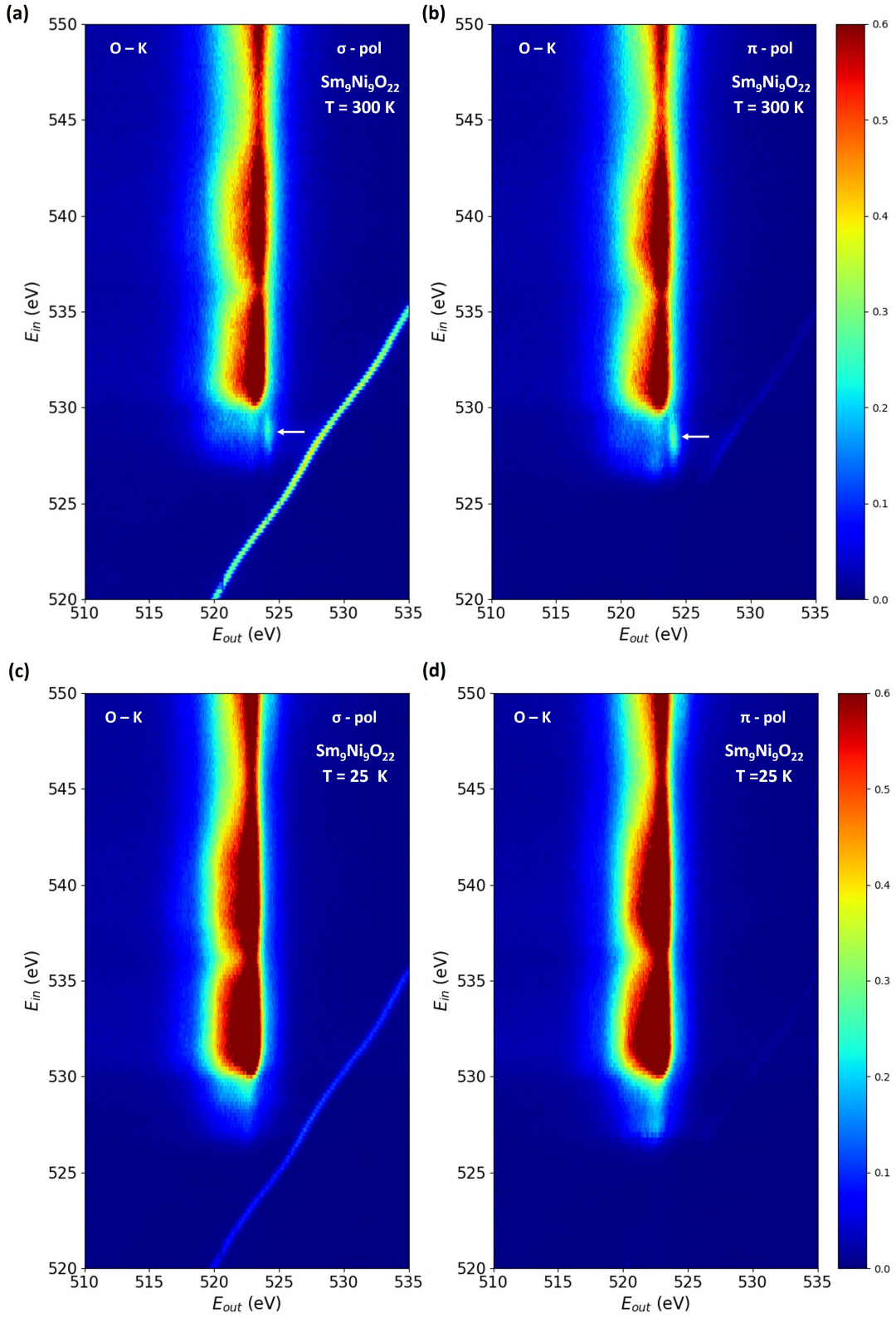

Figure S11: RIXS Map of O-K edge of $Sm_9Ni_9O_{22}$ showing the electronic transition at different temperatures.(a,b) RIXS map in incident (E_{in}) and detected (E_{out}) photon energy scales for (a) σ and (b) π incident photon polarisations at 300K, the low-energy loss fluorescence line is indicated by the white arrow. (c,d) RIXS map in incident (E_{in}) and detected (E_{out}) photon energy scales for (c) σ and (d) π incident photon polarisations at 25K.

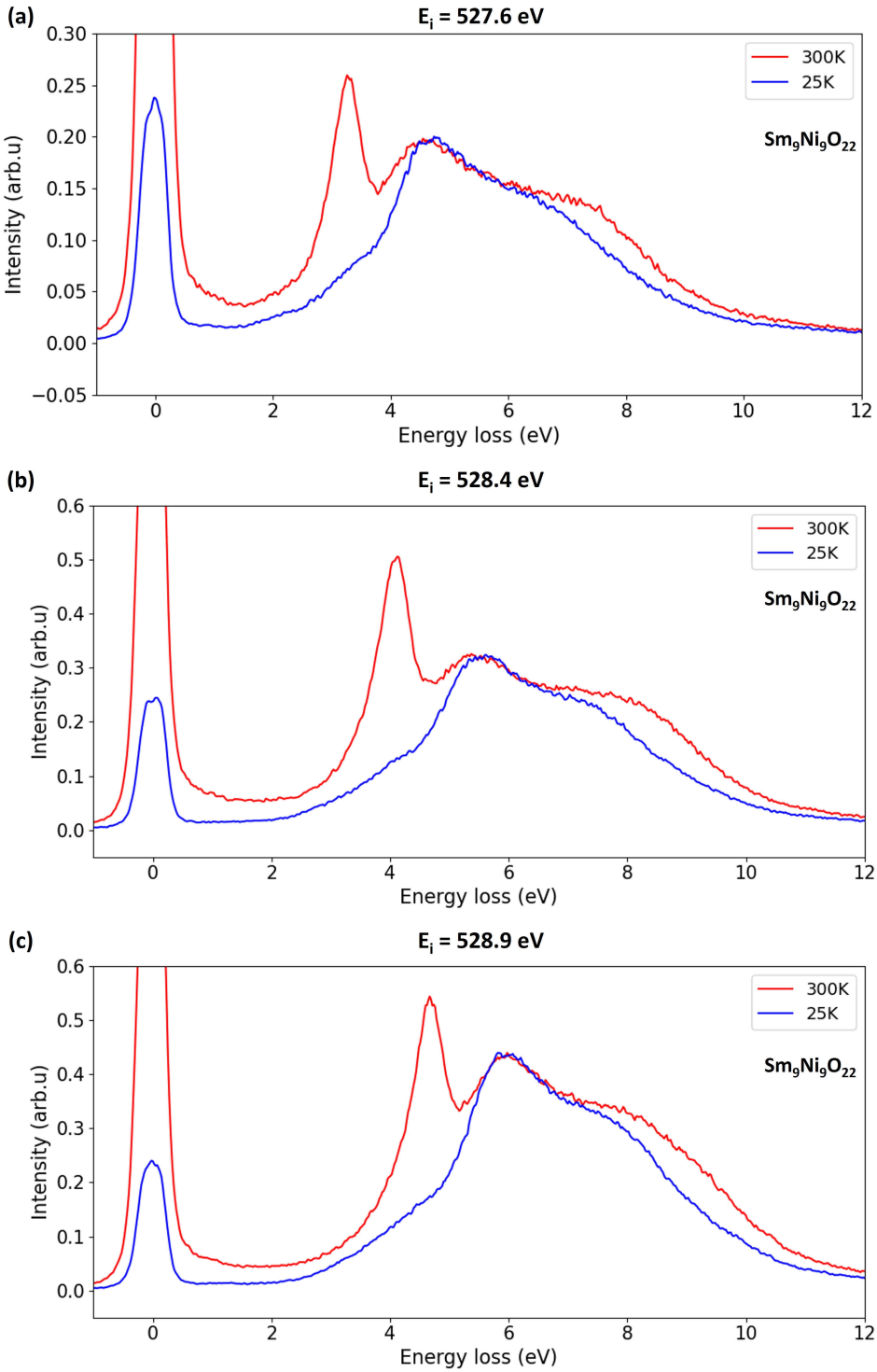

Figure S12: Temperature dependant RIXS line Profile of $Sm_9Ni_9O_{22}$ at different photon energies for the σ polarised incident photons. The spectra at an incident photon energy of (a) 527.6 eV, (b) 528.4 eV, and (c) 528.9 eV.

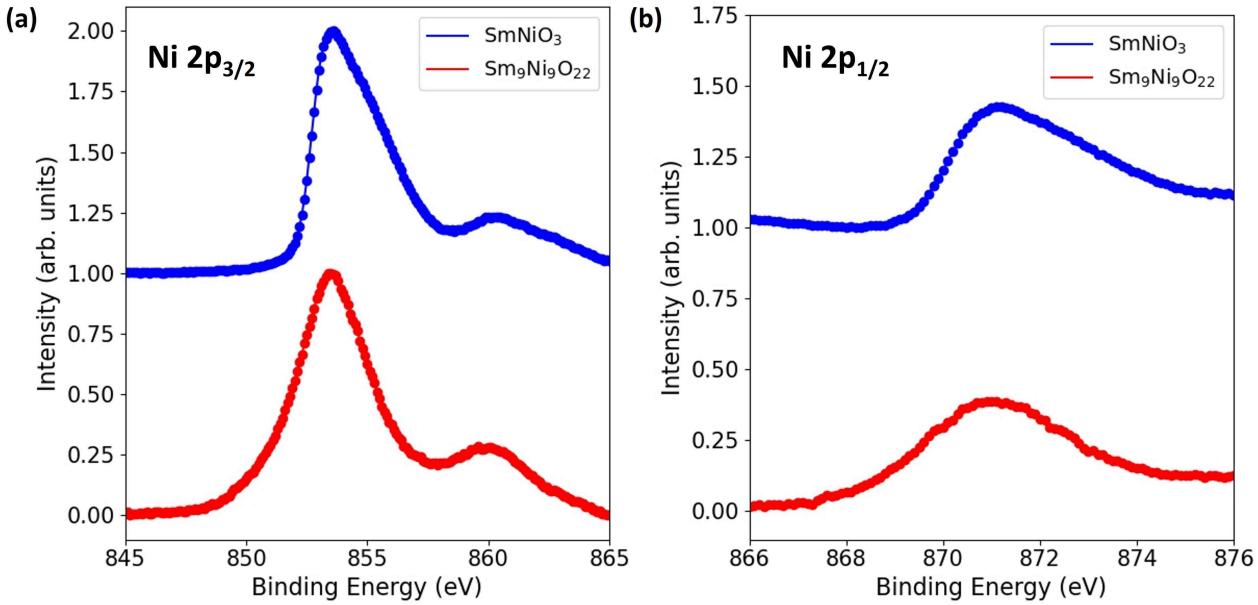

Figure S13: HAXPES comparison of $Sm_9Ni_9O_{22}$ and $SmNiO_3$ for (a) Ni $2p_{3/2}$ and (b) Ni $2p_{1/2}$ core levels. The measurements were done in a bulk sensitive mode, probing the whole thin-film. In both, $Sm_9Ni_9O_{22}$ has a low binding energy (LBE) shoulder, indicative of the Ni^{1+} in the square-planar sites. The bulk-probing capacity of HAXPES makes it insensitive to possible surface contaminations or artefacts. One noticeable difference is the presence of a low binding energy (LBE) shoulder for $Sm_9Ni_9O_{22}$ compared to $SmNiO_3$ that can also be attributed to the Ni^{2+} and Ni^{1+} sites.

4 Electronic structure simulations

The orbital occupancy, net spin polarization, and density of states of $Sm_9Ni_9O_{22}$ were calculated using DFT+U framework of Quantum ESPRESSO code [4, 5]. The DFT+U calculations were performed with a J = 1.2 eV, making $U_{effective}$ = U - J, on the symmetrized monoclinic $Sm_9Ni_9O_{22}$ unit cell given in Table S1. The Ni 3d orbital occupancy obtained for a U of 6 eV and a J of 1.2 eV is given in Table S2. It evidences the square-planar Ni site to be in a $3d^9$, pyramidal and octahedral Ni sites to be in a $3d^8$ occupancies. The corresponding spin-polarized density of states is shown in Figure S16.

The multiplet calculations were performed using CTM4XAS, CTM4RIXS [6], and Quanty [7]. The calculation for a D_{4h} Ni^{2+} was done in CTM4XAS and CTM4RIXS using the crystal field parameters $D_q = 0.13$ eV, $\Delta_t = 0.07$ eV, $\Delta_s = 0.15$ eV. The dichroic XAS results for the Ni-L edge are shown in Figure S14, and the RIXS results are shown in Figure 4 in the main text. Additionally, the RIXS map for a D_{4h} Ni^{1+} was done using Quanty, with $D_q = 0.13$ eV, $\Delta_t = 0.10$ eV, $\Delta_s = 0.30$ eV for the crystal-field parameters. The results are shown in Figure S15. From these, the obtained orbital energy level values are shown in Table S3.

Ni site	Spin	$\mathbf{d}_{x^2-y^2}$	$\mathbf{d}_{z^2}$	$\mathbf{d}_{xy}$	$\mathbf{d}_{xz}$	$\mathbf{d}_{yz}$
Square-planar	up	0.81	0.98	0.91	0.98	0.98
	down	**0.16**	0.97	0.77	0.97	0.98
Pyramidal	up	0.96	0.97	0.99	0.99	0.99
	down	**0.17**	**0.20**	0.98	0.98	0.99
Octahedral	up	0.98	0.98	0.99	0.99	0.99
	down	**0.13**	**0.16**	0.98	0.98	0.98

Table S2: Occupation of 3d orbital in different Ni sites in $Sm_9Ni_9O_{22}$ by DFT calculations with a Hubbard U parameter of 6 eV and Hund's J parameter of 1.2 eV. The absolute values of the results indicates a $3d^8$ occupancy for the pyramidal and octahedral Ni sites, with a $3d^9$ occupancy for the square-planar sites.

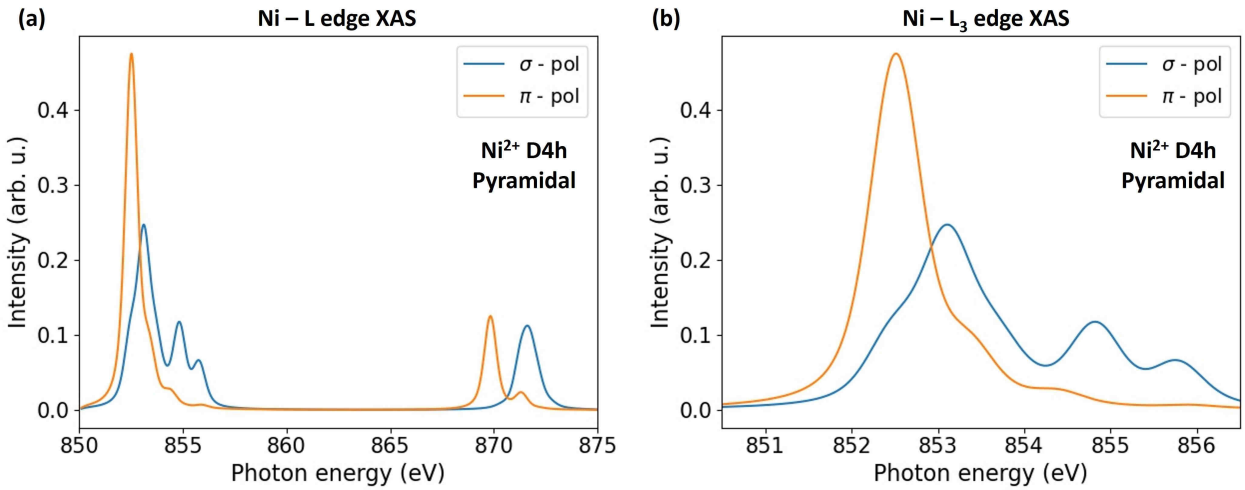

Figure S14: CTM4XAS [6] calculation of Ni^{2+} in D4h for the pyramidal sites. (a) Results for both polarizations for the Ni-L edge, (b) a magnified Ni-L_3 edge for both polarizations. It has been obtained using $D_q = 0.13$ eV, $\Delta_t = 0.07$ eV, $\Delta_s = 0.15$ eV for the crystal-field parameters. Same parameters are used for the RIXS calculations. It gives the following orbital energetic hierarchy : $E_{x^2-y^2}(b_{1g})$ = 0 eV (reference) ; $E_{z^2-r^2}(a_{1g})$ = - 0.95 eV ; $E_{xz/yz}(e_g)$= - 1.30 eV ; $E_{xy}(b_{2g})$= - 1.40 eV

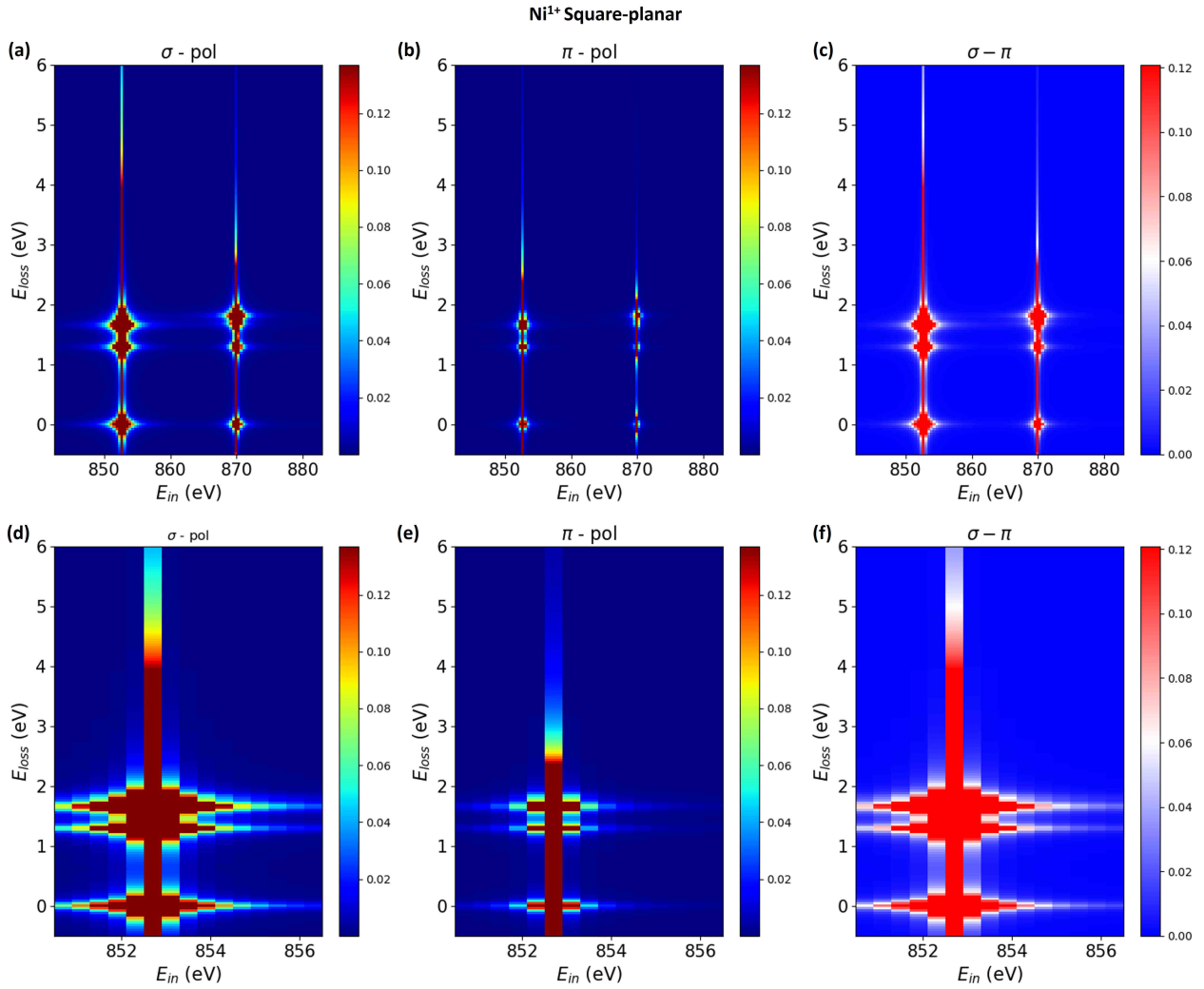

Figure S15: Calculated RIXS map at Ni-L edge of Ni^{1+} Square-planar sites by Quanty [7]. (a) Results for σ polarization, (b) π polarization, (c) Difference of both polarization ($\sigma - \pi$). (d-f) The magnified map at the Ni-L_3 edge. It has been obtained using $D_q = 0.13$ eV, $\Delta_t = 0.10$ eV, $\Delta_s = 0.30$ eV for the crystal-field parameters. It gives the following orbital energetic hierarchy : $E_{x^2-y^2}(b_{1g})$ = 0 eV (reference) ; $E_{xy}(b_{2g})$= - 1.30 eV ; $E_{z^2-r^2}(a_{1g})$ = - 1.70 eV ; $E_{xz/yz}$(eg)= - 1.70 eV.

Ni site	D_q	Δ_t	Δ_s	$E_{x^2-y^2}$	E_{xy}	$E_{z^2-r^2}$	$E_{xz/yz}$
Pyramidal	0.13 ev	0.07 ev	0.15 eV	0 eV	-0.95 eV	-1.30 eV	-1.40 eV
Square-planar	0.13 eV	0.10 eV	0.30 eV	0 eV	-1.30 eV	-1.70 eV	-1.70 eV

Table S3: Table showing the obtained energy level values for Ni^{2+} D_{4h} pyramidal and Ni^{1+} D_{4h} Square-planar sites from fitting the RIXS data using CTM4XAS and Quanty.

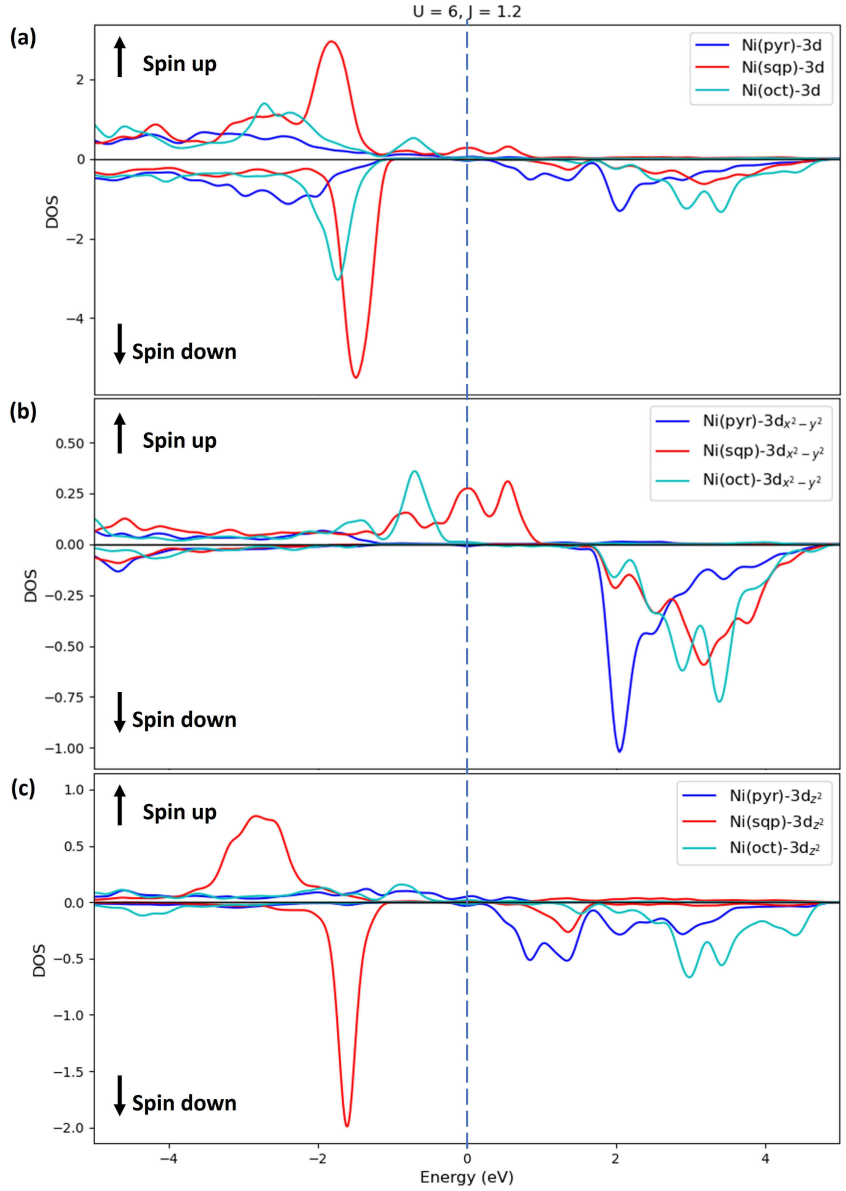

Figure S16: Partial density of states of different Ni sites in $Sm_9Ni_9O_{22}$ from DFT+U calculations, for U = 6 and J = 1.2 eV for (a) Total 3d orbital, (b) $3d_{x^2-y^2}$ orbital, and (c) $3d_{z^2}$ orbital. A first approximation is to consider the O-K edge as a probe of the unoccupied densities of state with O-2p character. The O-K pre-peak is then arising from the hybridization of the O-2p with the Ni-d band. When comparing the partial density of states above the Fermi level, alternating sequence of in-plane ($3d_{x^2-y^2}$), out-of-plane ($3d_{z^2}$) and in-plane ($3d_{x^2-y^2}$) states are legible, in agreement with the σ and π dependence of the XAS measurement.

References

[1] Moriga, Toshihiro, et al. ”Reduction of the perovskite-type LnNiO3 (Ln= Pr, Nd) to Ln3Ni3O7 with monovalent nickel ions.” Solid State Ionics 74.3-4 (1994): 211-217.

[2] Bisogni, V. et al. Ground-state oxygen holes and the metal–insulator transition in the negative charge-transfer rare-earth nickelates. Nature Communications 7, 13017 (2016)

[3] Meyers, D., et al. Pure electronic metal-insulator transition at the interface of complex oxides. Scientific reports 6.1: 27934.(2016).

[4] Giannozzi, P. et al. Quantum espresso: a modular and open-source software project for quantum simulations of materials. Journal of physics: Condensed matter 21, 395502 (2009)

[5] Giannozzi, P. et al. Advanced capabilities for materials modelling with quantum espresso. Journal of physics: Condensed matter 29, 465901 (2017)

[6] Stavitski, Eli, and Frank MF De Groot. ”The CTM4XAS program for EELS and XAS spectral shape analysis of transition metal L edges.” Micron 41.7 (2010): 687-694.

[7] Haverkort, M. W., M. Zwierzycki, and O. K. Andersen. ”Multiplet ligand-field theory using Wannier orbitals.” Physical Review B 85.16 (2012): 165113.